Stony Brook University

Photocatalyzed silver deposition on perovskite surfaces

A Thesis Presented

by

Benjamin Bein

to

The Graduate School

in Partial Fulfillment of the Requirements

for the Degree of

Master of Arts

in

Physics

Stony Brook University

August 2011

Stony Brook University

The Graduate School

Benjamin Bein

We, the thesis committee for the above candidate for the Master of Arts degree, hereby recommend acceptance of this thesis.

Matthew Dawber - Thesis Advisor

Assistant Professor, Department of Physics and Astronomy

Philip B. Allen

Professor, Department of Physics and Astronomy

Maria V. Fernandez-Serra

Assistant Professor, Department of Physics and Astronomy

This thesis is accepted by the Graduate School.

Lawrence Martin

Dean of the Graduate School

Abstract of the Thesis

Photocatalyzed silver deposition on perovskite surfaces

by

Benjamin Bein

Master of Arts

in

Physics

Stony Brook University

2011

In this thesis a simple model for the growth of silver particles on well defined surfaces is developed. The model is applied to introduce a new approach to compare the surface reactivity of different materials by estimating the amount of deposited silver from silver particle height. This technique was applied to investigate the differences in surface reactivity between ferroelectric $PbTiO_3$ and paraelectric $SrTiO_3$. The model suggests that the reactivity of $PbTiO_3$ is 50% higher than on $SrTiO_3$. Furthermore it has been shown that a $SrRuO_3$ bottom electrode under a $PbTiO_3$ film has no measurable effect on the surface reactivity of $PbTiO_3$.

Contents

List of Figures

List of Tables

Acknowledgements

I am heartily thankful to my supervisor, Professor Matthew Dawber; without his guidance, support and inspiring discussions I would not have finished this thesis. I am indebted to my colleagues, John Sinsheiner, Joseph Magee and Sara Callori for their support, suggestions and for proofreading the manuscript of this thesis.

I also want to thank my thesis committee, Professor Philip B. Allen and Professor Maria V. Fernandez-Serra My gratitude also goes to all my teachers and Professors during my undergraduate studies at Würzburg for showing me the beauty of physics, especially to my Bachelor advisor Professor Haye Hinrichsen.

I also would like to thank all my friends in Stony Brook, Wiesentheid and Würzburg, they always cheered me up.

Special thanks goes to my beloved family; Thank you for your love, support and advice.

Last but not least I would like to thank the *German Academic Exchange Service* (DAAD) for nine months of funding for this thesis.

1 Introduction

The energy hunger of modern society is growing every year. With time it was realized that this energy can not be supplied by fossil fuels for ever and in our days one big challenge is to find a way to replace fossil fuels by regenerative fuels. The largest known regenerative power supply is the sun (with 3.846×10^{26} W). There are many ideas to use a tiny fraction of this to supply power for mankind, such as photovoltaic cells or thermal solar power plants. Another approach to use sun energy is to split water into hydrogen and oxygen on semiconducting surfaces. The advantage of hydrogen production is that hydrogen storage and transport is simpler than that of electricity, and the hydrogen could be used either directly as a fuel or in the production of gasoline. But these water splitting devices still have some major problems. One of these problems is that most materials which can split water photocatalytically have a band gap which is close to or above 3eV. This means that only a small fraction of the sun light which is irradiated onto the earth can be used. Another problem is to transfer charge curriers to the surface without recombining electron-hole pairs. Both problems reduce the efficiency of these devices.

The first photocatalytic water splitting material to be discovered was TiO_2 in 1972 [4]. Since then many other materials were found to be photocatalytically active for water splitting. One of these materials is the perovskite crystal $SrTiO_3$. The surface reactivity of $SrTiO_3$ for water splitting is greater than TiO_2. Perovskites have a huge range of properties which can be accessed by changing the species the crystal is composed of. This makes them very interesting materials for photocatalytic water splitting.

This thesis tries to increase the understanding of surface and crystal properties to increase the efficiency of future water splitting devices. Therefore the photocatalytic deposition of silver from a silver nitrate solution was investigated. This reaction is a probe reaction for water splitting and can help to understand the water splitting process in more detail

2 Ferroelectrics

The special property of a ferroelectric material is its *spontaneous polarization*, which means the material has a switchable, non-zero polarization in zero electric field. Ferroelectrics are also pyroelectric, piezoelectric and insulating[21]. The best known ferroelectric atomic structure is the perovskite oxide structure. The first perovskite oxide ($BaTiO_3$) with ferroelectric properties was discovered in 1945[37]. In the following, perovskites will be described in more detail.

2.1 Perovskite oxides

The first perovskite crystal discovered was $CaTiO_3$. It was found by the German mineralogist Gustav Rose in the Ural Mountains (1839) and was named after the Russian mineralogist L. A. Perovski. The composition of the perovskite structure is ABO_3, where A and B are different cation elements or a mixture of two of those elements (e.g. $Ba_{1-x}Sr_xTiO_3$). The possible number of valence electrons of the A atoms lies between +1 and +3 and for the B atoms between +3 and +6. Perovskites are materials with a wide range of properties. They can be metals, antiferromagnetic, ferromagnetic, insulators, ferroelectric, parraelectric, multiferroic or superconducting. This number of possible properties makes perovskites extremely interesting for material engineering. These numerous properties are possible because of dislocation, distortion, tilting, rotations, etc. of the oxygen atoms from the ideal structure.

2.1.1 Ideal pervoskite structure

The ideal perovskite oxide structure can be described by two alternative ways of representing the cubic unit cell. In one representation the A atoms are in the corners of the cell and the B atoms are in the center, surrounded by six oxygen atoms on the center of each surface; In the other representation the B atoms are in the corners and the A atoms are in the center of the unit cell, with oxygen atoms at the midpoint of each edge. Both unit cells are shown in Fig. 1. This is the high-symmetry perovskite reference structure and has a simple cubic lattice with a five atom basis and the space group $Pm\overline{3}m$. The high-symmetry structure is not ferroelectric, but it is the high temperature paraelectric phase for most ferroelectric perovskite oxides. There are two different ways to induce ferroelectricity into the perovskite structure, the A-and B-site

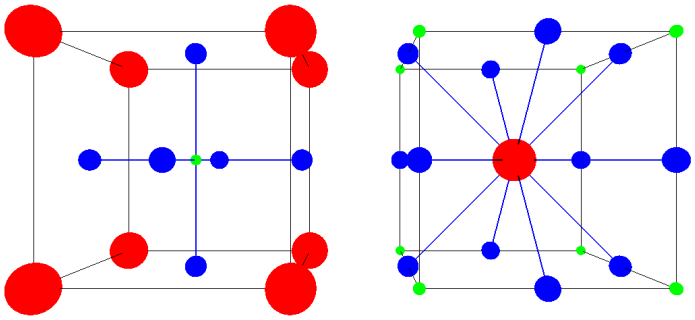

Figure 1: ABO_3 unit cell from two different view points. In the left part of the picture the B atom (green) is in the center of the unit cell and surrounded by six O atoms (blue), in the right part of the picture the A atom (red) is in the center of the unit cell and surrounded by twelve O atoms (blue)

driven ferroelectrics.

2.1.2 A-and B-site driven perovskites

To understand the mechanisms which force the perovskite oxide structure to be ferroelectric, one should first have a look at the stability of the high symmetry perovskite structure. In 1926 Goldschmidt[8] introduced a model based on ionic radii, which supports the stability of the perovskite structure by an empirical criterion. His model is based on the following two rules:
(i)a cation will be surrounded by as many anions as can touch it, but no more.
(ii)all the anions must touch the cations and the anion-cation distance is obtained by the size of the oxygen octahedron.

For the perovskite this leads to a rule for the ideal relation between ionic radii:

$$r_A + r_O = \sqrt{2}\,(r_B + r_O) \tag{1}$$

with r_A as the radius of the A-site atoms, r_B as the radius of the B-site atoms and r_O as the radius of the oxygen atoms.

Real perovskites will, in general, not satisfy this rule. Therefore the tolerance factor t is

defined to measure the deviation from the ideal radii:

$$t = \frac{r_A + r_O}{\sqrt{2}\,(r_B + r_O)} \tag{2}$$

The perovskite structure is only maintained if $t \approx 1$, otherwise another ABO_3 structure will be formed. If one assumes for $SrTiO_3$ the atomic radii 1.379Å for Sr, 0.807Å for Ti and 1.502Å for O (radii from[32], used for first principles calculations), the corresponding t=0.88. For $t < 1$ the A atom is too small for the hole between the oxygen octahedrons. Therefore it can not support an equal bond to all twelve neighboring O atoms. This perovskites are called A-site driven perovskites. Most of the A-site driven perovskites are not ferroelectric (e.g. $SrTiO_3$) and have rotations or tilting of the oxygen octahedron. $PbTiO_3$ is an exception to this rule and has a dislocation of the oxygen octahedron and the B-atom, which results in a dislocation of the positive charge center in respect to the negative charge centers and is shown in Fig 2. If $t > 1$ the B atom is to small for the hole in the center of the oxygen octahedron. In this case the A-O distance defines the structure. This perovskites are called B-site driven perovskites. In a B-site driven perovskite the ferroelectricity is induced by the displacement of the B-atom from the ideal structure(e.g. $BaTiO_3$). This leads also to a displacement of the positive center of charge compared to the negative center of charge.

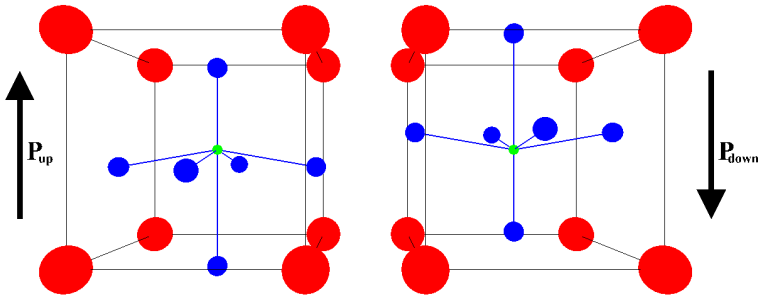

Figure 2: Microscopic picture of a spontaneous polarized $PbTiO_3$ perovskite. The red spheres are the A-atoms (Pb), the green spheres are the B-site atoms (Ti) and the blue spheres are the oxygen atoms. In the left cell the polarization is "up" and in the right it is "down"

2.2 Properties of ferroelectrics

As mentioned at the beginning of this section, the spontaneous polarization is the indicating property of a ferroelectric material. To measure the polarization of a ferroelectric material one can perform a hysteresis loop which is shown in Fig. 3. This figure starts with an unpolarized sample at (1). When an electric field is applied the polarization grows rapidly with the increasing electric field until it reaches the saturated point (2). After saturation the increase of the polarization with increasing electric field is only driven by electric charging (3). After a reduction of the electric field to zero the sample now stays polarized (4). At this point the remaining polarization is the *remanent polarization* $+P_R$. By applying an electric field in the opposite direction, the polarization at first changes only by a small amount. When the applied field reaches E=-E_C (the *coercive field*) the polarization abruptly flips (5). Increasing the applied field further, one reaches the saturated region again (6). Reducing the electric field to zero leads to the polarization -P_R. To find $+E_C$ one has to increase the field again in the positive direction. The linear extrapolation of the saturated region to zero electric field is the *spontaneous polarization*.

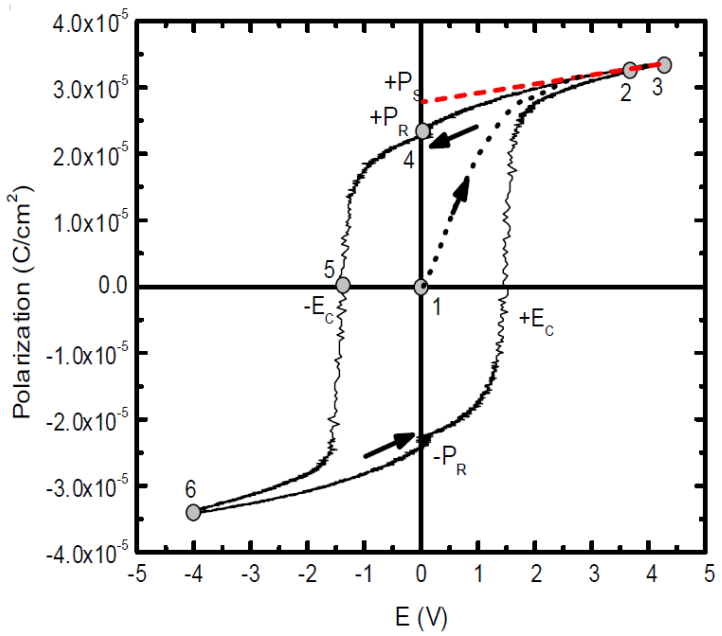

Figure 3: Hysteresis loop of a $Pb(Zr,Ti)O_3$ Samsung sample. The spontaneous polarization P_S is the linear extrapolation of the saturated region and the remanent polarization P_R is the polarization at zero field if one comes from one of the saturated regions.

With decreasing temperature most ferroelectrics have a phase transition from a paraelectric phase to a ferroelectric phase. When a material undergoes this transition from its paraelectric phase the polarization of each unit cell does not have to point in the same direction. The material will build up regions in which the spontaneous polarization of all unit cells point in the same direction. These regions are called ferroelectric *domains*. Between two domains is a small region which does not belong to either of the domains and is called a *domain wall*. The preferred direction of the spontaneous polarization depends on the mechanical or electrical boundary conditions. Fig. 2 shows a microscopic view of two stable polarization states in $PbTiO_3$ and Fig. 4 shows a macroscopic view of the domains and domain walls.

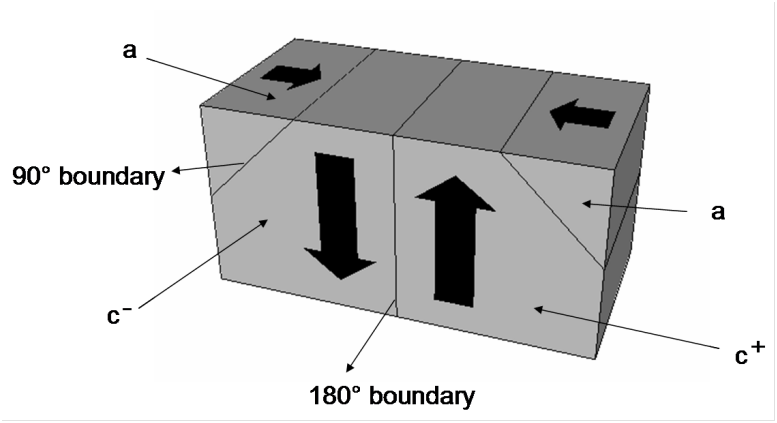

Figure 4: Macroscopic view of domains and domain walls in a ferroelectric crystal. c^+ and c^- domains are polarized out of plane and a domains are polarized in plane.

Domains with a polarization out-of-plane are either called up (c^+) or down (c^-) domains, depending on the direction of their polarization (see Fig. 4). In-plane domains are called a domains[29]. The a-c domain walls are 90° boundaries and the c^+-c^- domain walls are 180° boundaries. Only the 90° domain walls can release stored elastic energy. Both domain wall types occur to minimize the depolarization field.

The *depolarization field* is the electric field which is the consequence of the electric dipole. It tries to move the ions to a position in which no electric dipole is formed. A ferroelectric has a equilibrium between the long range electrical forces from the depolarization field and the short range atomic repulsion forces. The depolarization field can be reduced by screening.

2.3 Screening

A ferroelectric material is nearly always screened when it is at equilibrium. The only case where a unscreened surface occurs is in high vacuum conditions. The screening charge σ_S has the opposite polarity to the underlying dipole charge σ_P. Four different screening states can be observed [29].

- Completely unscreened surface ($\sigma_S = 0$).
- Over-screened surface ($\sigma_P < \sigma_S$).
- Partially screened surface ($\sigma_P > \sigma_S$).
- Completely screened surface ($\sigma_P = \sigma_S$).

The completely unscreened surface is energetically unfavored and occurs only in high vacuum. An over-screened surface is also unfavored but can be observed after switching a domain[30]. Mostly on surfaces one observes a partial or complete screening. There are two different screening mechanisms[10].

The first one is the screening by intrinsic free charge carriers (*internal screening*) . The free charge carriers are forced to move to the surface of the ferroelectric material by the depolarization field. This introduces a charge distribution at the surface and in the first layers of a thin film. One can also describe the internal screening by band bending at the surface of ferroelectric materials. Since ferroelectric materials are insulating there is only a low amount of free charge carriers. Therefore usually the degree of intrinsic screening is much less than the following external screening.

The second mechanism is the screening by external molecules (*external screening*) . The most common molecule for external screening is water. Water screens a ferroelectric surface either through its dipole moment or by dissociation into OH and H at the surface. In nature both possibilities occur, but the dissociation is favorite at polar surfaces. After water is dissociated, the H binds to a surface O atom and the OH binds to a surface metal atom. First principles studies on out-of-plane polarized $PbTiO_3$ show that OH and O adatoms, adsorbed to a surface Pb atom, stabilize a polarization pointing out of the surface (c^+). However H binds to surface O atoms and preserve polarization pointing into the surface (c^-). Undissociated H_2O binds

only weakly to the unpolarized surface[24]. First principles calculations and in situ electron diffraction experiments also show that in-plane polarization supports water dissociation on a ferroelectric $BaTiO_3$ surfaces[5, 25].

If the material is in a environment without enough external screening molecules, the surfaces tend to a 180° stripe domain structure to reduce the depolarization field inside the ferroelectric material[13]. Fig. 5 shows a schematic view of a ferroelectric material with its polarization P, depolarization field E_D, internal screening E_{Si} and external screening E_{Se}.

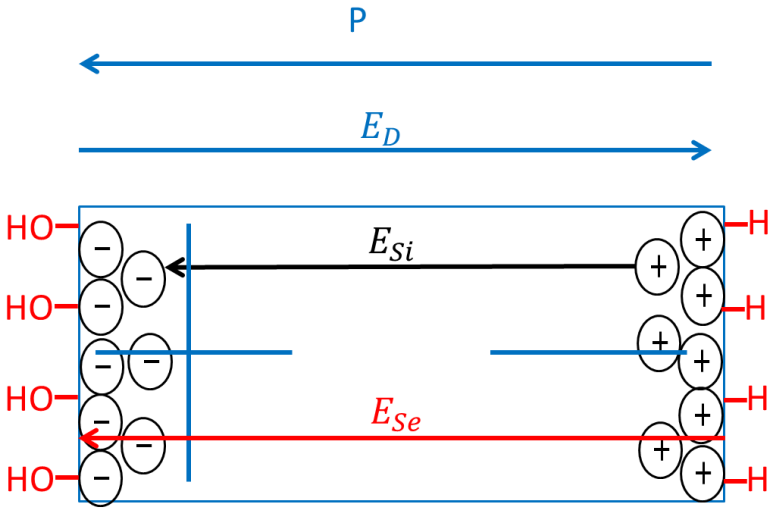

Figure 5: Schematic view of a screened ferroelectric. Blue is the permanent dipole charge σ_P of the ferroelectric and the depolarization field E_D. The internal screening by free charge carriers is illustrated in black, with its corresponding screening field E_{Si}. Adsorbed adatoms are red and they cause the external screening E_{Se}. The screening charge σ_S is a combination of intrinsic and external charges.

2.4 Materials

All materials studied in this work have the perovskite structure, but they all have different electrical properties and different surface structures. It is important to know as many physical properties of the materials as possible to find connections between their physical and chemical properties.

2.4.1 $PbTiO_3$

$PbTiO_3$ is a A-site driven ferroelectric. The displacement of the B atom (Ti) and the oxygen octahedron from the perfect perovskite structure leads to a displacement of center of the mass of the positive cations (Pb, Ti) and the negative anions (O), which results in a dipole moment. The critical temperature between the cubic (a=b=c=3.969Å), paraelectric phase and the ferroelectric, tetragonal (a=b=3.904Å, c =4.152Å) phase is at 760K. The spontaneous polarization of $PbTiO_3$ can be up to $75\mu C/cm^2$. First principles calculations predict that only the PbO surface of $PbTiO_3$ is thermodynamical stable[16]. X-ray scattering reveals that there is a surface reconstruction of the top TiO_2 layer with a $c(2\times2)$ and a 10° counter rotation of the oxygen cage around the Ti atom[18]. There might be a surface PbO layer, without any reconstructions, above the reconstructed TiO_2 layer. This would bring the theoretical prediction in harmony with experiment. The optical band gap of $PbTiO_3$ is 3.6eV [17]

2.4.2 $SrTiO_3$

$SrTiO_3$ is a cubic (a=b=c=3.905Å) perovskite and is paraelectric at room temperature. It is easily polarizable by an electric field. At a temperature of 110K $SrTiO_3$ undergoes a tetragonal phase transition but does not become ferroelectric in bulk. Ferroelectricity can be induced in $SrTiO_3$ by strain engineering[9]. In this work TiO_2 terminated $SrTiO_3$ was mainly used as a substrate because of the small lattice mismatch with the in-plane lattice parameters of $PbTiO_3$ ($< 0.01\%$) and $SrRuO_3$ (0.6%). The use of a $SrTiO_3$ substrate leads furthermore to a out-of-plane directed polarization for a $PbTiO_3$ sample. For $SrTiO_3$ both surfaces (TiO_2 and SrO are thermodynamically stable [16]. The direct band gap of $SrTiO_3$ is 3.75eV and its indirect band gap is 3.25eV [32]

2.4.3 $SrRuO_3$

$SrRuO_3$ is a metallic perovskite and has an orthorhombic structure(a=5.53Å, b=5.57Åand c =7.85Å) with a lattice distortion angle between[110] and $[\bar{1}10]$ in the (001) plane of 89.6°. $SrRuO_3$ has a ferromagnetic phase below 155K and can be considered as pseudo-cubic structure (a=b=c=3.93Å). Thin film growth experiments suggest that $SrRuO_3$ is RuO terminated[23].

This comes from a increased growth time for $SrRuO_3$ during the first layer on a TiO_2 terminated $SrTiO_3$ substrate. $SrRuO_3$ is often used as an electrode for electrical contact of thin films; therefore this work investigates the influence of a $SrRuO_3$ bottom electrode on the chemical reactivity of the film above it.

3 Water splitting

The best known way to split water is electrolysis. In this approach two electrodes are placed under water and a voltage is applied between the two electrodes. Oxygen forms at the Anode and hydrogen at the cathode. Electrolysis has an efficiency of up to 80% for converting electrical energy into hydrogen gas. Another method for water splitting is photocatalysis. In the photocatalytical approach one irradiates materials, which are catalysing the water splitting reaction, with light. These materials can use the energy of the light to split water on their surface.

3.1 Water Spliting in general

Water splitting is a redox reaction. A redox reaction can always be split into two half reactions. One part is the reduction and the other part is the oxidation. There are many different possible redox reactions for water spitting: the easiest example is:

$$\begin{aligned} \text{(oxidation): } 2\mathrm{H_2O_{(aq)}} &\rightarrow \mathrm{O_{2(g)}} + 4\mathrm{H^+_{(aq)}} + 4\mathrm{e^-} \qquad \mathrm{G^0} = 4 \cdot 1.23eV \\ \text{(reduction): } 2\mathrm{H^+_{(aq)}} + 2\mathrm{e^-} &\rightarrow \mathrm{H_{2(g)}} \qquad \mathrm{G^0} = 0.00eV \end{aligned} \tag{3}$$

This redox reaction pair can be combined to obtain the general reaction of water splitting:

$$2\mathrm{H_2O_{(aq)}} \rightarrow \mathrm{O_{2(g)}} + 2\mathrm{H_{2(g)}} \qquad \mathrm{G^0} = 4 \cdot 1.23eV \tag{4}$$

Unfortunately water splitting is an endothermal reaction and one has to add energy to the reactants. The energy needed for each single H is called the enthalpy, $\mathrm{G^0}$=1.23eV, at standard conditions for temperature and pressure (T=25°C, P=1atm). To split water into $\mathrm{H_2}$ and $\mathrm{O_2}$ not only the enthalpy is needed, one needs also an activation energy.

Different approaches are developed to add this energy to the reaction. One is electrolysis, where the needed energy is added by an electrical bias. Another is by thermal decomposition; here the water is heated up to temperatures of 2200°C and higher. At these high temperatures the water molecules dissociate into, among other products, $\mathrm{H_2}$ and $\mathrm{O_2}$. Furthermore water can be split by using photocatalytic materials. When these materials get irradiated by UV or visible light, they use the photon energy to split water on their surface . The surface also influences

the needed activation energy, in particular how likely H^+ or OH^- ions adsorb on the surface and how easily charge is transferred to the adsorbed ions.

3.2 Photocatalytic water splitting

There are several different approaches for using light to split water. One approach is to use photovoltaic cells to produce electricity, which is used in a electrolysis process to produce oxygen and hydrogen. Another approach is to use photoabsorbing particles, where the entire water splitting process takes place on one catalytic nano particle. The approach which this work is following is photocatalytic electrolysis, where light adsorbing semiconductors are one or both electrolysis electrodes and the water splitting reaction takes place on their surface. Review papers can be found in references [14] and [15].

For photocatalysis one can use two different systems. The more complex, is a two semiconductor system. Both electrolysis electrodes are semiconductors and illuminated, so that the necessary band gap is lower than in a single semiconductor approach. Therefore a greater efficiency is possible in the two semiconductor system than in the single semiconductor system. In the single semiconductor approach one illuminates only the semiconductor electrode and uses a dark (not illuminated) counter electrode. Fig. 6 shows the schematically set up of a single photoelectrode system.

The first discovered single photoelectrode water splitting system was a n-type TiO_2 semiconductor with a band gap of $\sim$3eV in 1972 [4]. Since then substantial work has been done on this and other materials and is summarized in many review papers (e. g. [29] and [22]).

For solar water splitting there are several requirements the semiconductor has to satisfy:

- It needs a large enough band gap to provide the necessary energy. In the ideal case this would be 1.23eV, which corresponds to a wavelength of $\sim$1000nm. For a real system the band gap should be around 2.0ev[3]- 2.5eV [22]

- The valence band must lie under the potential of the oxidation of water (eq. 3) and the conduction band must be greater than the reduction potential of hydrogen (eq. 3). Fig. 7 shows a scheme of the necessary band structure.

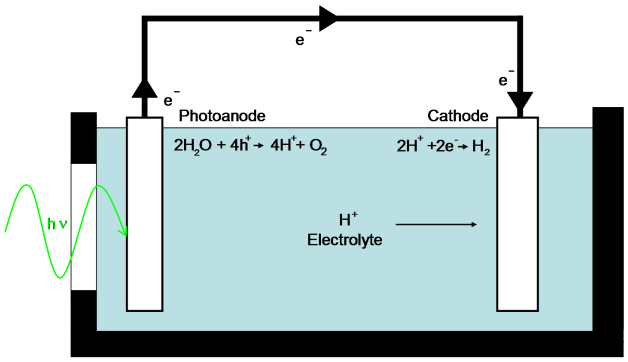

Figure 6: Schematic set up of a single photoelectrode system. The left electrode gets illuminated through a window by photons with the energy hν. Here the photogenerated holes oxidize H_2O to O_2 and the photo generated electrons get transfered through a wire to the dark counter electrode. At this electrode H^+ gets oxidized to H_2

- It has to be inert to water. This means that the semiconducting surface does not get oxidized by water during the water splitting process.
- To provide the charge carriers for the water splitting reaction, the semiconductor needs a mechanism to transport the holes and electrons to the surface without recombining them.
- The surface of the semiconductor has to be a catalyst for the water splitting process to reduce the necessary activation energy.

The perovskite materials introduced in section 2.4 have most of the required properties. For example $PbTiO_3$ and $SrTiO_3$ have both a large enough band gap ($SrTiO_3$ $E_g \approx 3.25$[32], $PbTiO_3$ $E_g \approx 3.6$[17]). For the (001) surface plane $SrTiO_3$ has a TiO_2 terminated surface, which is known to be inert against water and is a catalyst for the water splitting reaction [22]. For $SrTiO_3$ it is already known that its valence band lies under the potential of the oxidation of water and the conduction band lies over the reduction potential of hydrogen [7]. On $BaTiO_3$, another ferroelectric perovskite oxide, the different ferroelectric domains spatially divide the generated charges [6].

Combining these traits, one can say that perovskite oxides are materials which sound promising for photocatalytic water splitting. They might be used in a system where both or only one

electrode is illuminated. It also might be possible to do the entire water splitting reaction on only one ferroelectric surface. This is due to the fact that different polarization directions(different domains) get screened by different adsorbents (see sec. 2.3). The biggest issue for ferroelectrics is the efficiency of the water splitting process. Therefore one can try to increase the catalytic effect of the surface and increase the mechanism which divides and transports the charge carriers to the surface. To increase the efficiency under sunlight one has to reduce the band gap without inducing recombination centers.

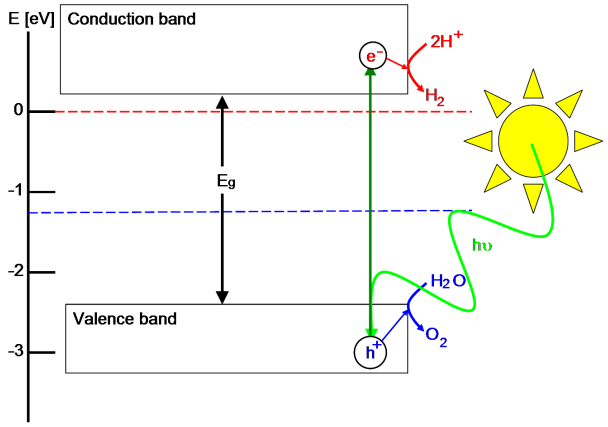

Figure 7: Schematic of the band structure of a semiconductor and the water splitting process. Light with the photon energy hν gets adsorbed by the material and induces an electron hole pair. The electron now can induce the oxidation of H^+ to H_2 and the hole the reaction from H_2O to O_2.

3.3 Water splitting efficiency

For every water splitting system efficiency is important. The efficiency of a water splitting semiconductor is limited by a number of factors, which are related to the band gap E_g of the semiconductor[1]:

- Only photons with a energy $E_{Ph} \geq E_g$ can generate electron-hole pairs. All other photons are 'lost'(in the sense of photocatalytic water splitting) energy.
- If the photon energy is greater than the band gap ($E_{ph} > E_g$) the excess energy $E_{ph} - E_g$ excites phonons and heats up the semiconductor and is not usable for the water splitting

process

- During the illumination of the semiconductor electron-hole pairs are created. These pairs have to be separated and transported to the surface of the semiconductor to be available for the water splitting process. During the transportation some electron-hole pairs will recombine reducing the efficiency.
- Only a fraction (∼75%) of the excited state energy can be used for the water splitting process. The reason for this is that the excited state is an internal energy but for water splitting one needs a free enthalpy. The excited states are a small number of states in a sea of ground states so that there is a loss of usable energy to entropy.

By considering these points one can define the efficiency of a water splitting semiconductor by[3]:

$$\eta_C = \eta_g \eta_{chem} \Phi_{conv} \tag{5}$$

where η_g is the usable part of the incoming solar radiation and is defined in (6), η_{chem} is the chemical efficiency and is defined in (8) and Φ_{conv} is the quantum yield of the water splitting process. This is the fraction of the excited electron hole pairs which do not recombine.
η_g is the usable part of the incoming solar radiation, with $E_{Ph} \geq E_g$ and can be expressed by:

$$\eta_g = \frac{J_g E_g}{E_S} \tag{6}$$

with E_S is the absolute incoming radiation power ($\frac{W}{m^2}$) and J_g is the absorbed photon flux ($\frac{1}{sm^2}$). J_g follows the equation:

$$J_g = \int_{\lambda_{min}}^{\lambda_g} \frac{\lambda \cdot \rho_{Ph}}{c \cdot h} \mathrm{d}\lambda \tag{7}$$

ρ_{Ph} is the spectral irradiation density($\frac{W}{m^2 nm}$), c is the speed of light, h is the Planck constant, λ_{min} is the minimal wavelength which the irradiation source emits and λ_g is the wavelength which corresponds to the semiconductor energy gap $\lambda_g = \frac{hc}{E_g}$.
η_{chem} is the chemical efficiency and reflects the fraction of the chemical stored energy to the energy of the exited electron hole pairs. It can be expressed through:

$$\eta_{chem} = \frac{E_g - E_{loss}}{E_g} \tag{8}$$

with E_{loss} as the energy loss per molecule in the water splitting process. From a entropic view E_{loss} has a minimum value of $\sim 0.3\text{eV} - 0.4\text{eV}$

This consideration leads to maximal efficiency of a water splitting semiconductor of $\sim 17\%$ with an estimated value of $E_{loss} = 0.8\text{eV}$ and the optimal band gap of $E_g = 2.0\text{eV}$. This efficiency gets further reduced by reflection, the transmission of incoming photons, and losses of gas during its collection.

3.4 Silver nitrate($AgNO_3$)

Silver nitrate is a white crystalline solid and dissolves easily in water into Ag^+ and NO_3^- ions. It can be used as a probe reaction for the oxidation part of the water splitting reaction (eq. 4). To do so one places a material into a silver nitrate solution and illuminates it. If during the illumination solid silver is deposied, then the material is photocatalytically active. Silver deposition can be described by two half reactions:

$$\begin{aligned} \text{(oxidation): } 2\text{H}_2\text{O}_{(\text{aq})} &\rightarrow \text{O}_{2(\text{g})} + 4\text{H}^+_{(\text{aq})} + 4\text{e}^- \qquad \text{G}^0 = 4 \cdot 1.23eV \\ \text{(reduction): } \text{Ag}^+_{(\text{aq})} + \text{e}^- &\rightarrow \text{Ag}_{(\text{s})} \qquad \text{G}^0 = 0.80eV \end{aligned} \tag{9}$$

The standard reduction potential of the reduction reaction from (eq. 9) is 0.80eV. On the other hand the standard reduction potential of $2\text{H}^+_{(aq)} + 2\text{e}^- \rightarrow \text{H}_{2(g)}$ is defined as 0.00eV. This means that the deposition of silver needs much less energy than the evolution of hydrogen gas and that the reaction (eq. 9) is easier than the complete water splitting reaction (eq. 4). The second part of the reduction of both reactions is the same, therefore one can check with the deposition of silver if a material has a valence band which is low enough to split water into oxygen and hydrogen ions. With the silver nitrate reaction one can not check if a material is able to reduce H^+ ions to H_2. To check if the material is also able to reduce H^+ one needs to employ a different probe reaction.

3.5 Visible light reactivity of doped $SrTiO_3$

There is already some literature which reports on silver deposition on doped $SrTiO_3$. In most of these experiments the authors measured the O_2 or H_2 gas evolution and tried to increase the efficiency of photo catalytic water splitting reaction under visible light irradiation. They used $AgNO_3$ as a proof reaction for O_2 evolution and a methanol solution as proof reaction for H_2 evolution. One approach to reduce the band gap of $SrTiO_3$ is to dope it with noble metals.

Doping $SrTiO_3$ with Cr to form $SrTi_{1-X}Cr_XO_3$ increases the absorption in the visible spectrum but also induces recombination centers for the electron hole pairs[11]. To reduce the recombination rate again one can codope $SrTiO_3$ with Cr and Sb to form $SrTi_{1-X-Y}Sb_XCr_YO_3$. In this mixture there are no Cr^{-6} ions which increase the recombination rate more than Cr^{-3} ions[11]. Another way to avoid Cr^{-6} ions in doped $SrTiO_3$ is to replace the Sr ions by Cr ($Sr_{1-X}Cr_XTiO_3$) instead of the Ti ions ($SrTi_{1-X}Cr_XO_3$) [34]. DFT calculations show that the band gap for Cr doped $SrTiO_3$ should be reduced by $\sim$0.4eV[36], depending on the doping concentration. A shift of the band gap by $\sim$0.4eV would result in a $\sim$2.8eV band gap for Cr doped $SrTiO_3$.

Besides Cr doping there are experiments which used Ni and Ta or Nb [19] and showed that one can get a visible light response by doping with Ni but the Ni doped $SrTiO_3$ showed a $\sim$ 15 times lower reactivity under UV light irradiation than plane $SrTiO_3$. Another work doped $SrTiO_3$ with Mn, Ru, Rh or Ir [12] and got visible light response for either O_2 or H_2 evolution.

The substrate effect on noble metal doped $SrTiO_3$ was also investigated [20] and showed that the silver deposition gets enhanced on V doped $SrTiO_3$ on Nb doped $SrTiO_3$ substrate; compared to the deposition of V doped $SrTiO_3$ on a $LaAlO_3$ substrate. It was also shown that Nb doped $SrTiO_3$ is not only reducing Ag^+ ions to Ag atoms but can also oxidize Ag^+ ions to form $Ag_7O_8NO_3$ from a $AgNO_3$ solution[28]. Another approach to reduce the band gap of $SrTiO_3$ is a mixture of $(AgNbO_3)_{3-x}(SrTiO_3)_x$[33]. This material shows the highest efficiency for x=0.25 under visible light irradiation ($\lambda \geq 410$nm). Furthermore the deposition of silver nanocrystals on $SrTiO_3$ can enhance the photo catalytic activity of $SrTiO_3$[26].

4 Experimental techniques

In this section it is discussed how to grow samples and how to characterize them. First Off-axis RF magnetron sputtering is described. This is followed by a short explanation of X-ray diffraction techniques, with which one can determine the quality and thickness of thin films. Finally, atomic force microscopy (AFM) was used for topological characterization of samples and for comparison of the silver deposition on different samples.

4.1 Off-axis RF magnetron sputtering

All samples were grown with an off-axis RF magnetron sputtering technique, which is a physical vapor deposition technique. Other physical vapor deposition techniques are pulsed laser deposition (PLD) and molecular beam epitaxy (MBE). All these techniques are well described in [21]. Here we will only give a short overview on the off-axis RF magnetron sputtering.

In the off-axis RF magnetron sputtering geometry (see Fig. 8) one has a radio frequency

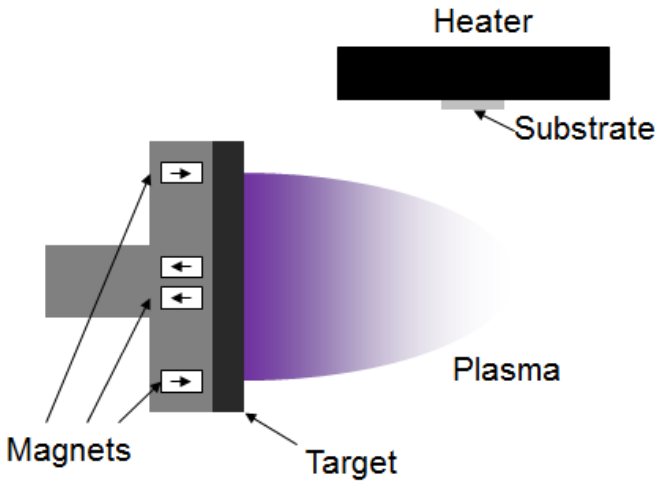

Figure 8: Schematic of the off-axis RF magnetron sputtering arrangement. The argon plasma particles hit the target and strike out material for the deposition on the substrate. The magnets increase the sputtering rate and the off-axis geometry reduces the resputtering of the film.

ac voltage between the target and the rest of the chamber. The chamber is defined as zero

potential and grounded. The target is made out of a ceramic which has the same stoichiometric composition as the desired film. Behind the target, strong permanent magnets are used to constrain the plasma and increase the sputtering rate. The substrate is fixed on a heater and is arranged at a 90°angle to the target to minimize resputtering of the sample. All these components are placed in a vacuum chamber to control the pressure and the gas mixture in which the film is grown.

During the sputtering process the vacuum chamber is filled with a sputtering gas (argon in this chamber) and, if an oxide is grown, also with oxygen to keep the film oxidized. The sputtering gas gets ionized by the RF voltage, but only the electrons can react to the high frequency field, the argon ions are too heavy. The electrons concentrate in front of the target and build up a DC bias, because the cathode (target) is smaller than the anode (rest of the chamber). The argon ions get accelerated towards the target by this bias. The actual sputtering process takes place when the argon ions hit the target and strike the surface atoms out of the target. These atoms deposit on the substrate and build up the film.

It is important to presputter a target every time one changes any sputtering parameter or changes the target. During presputtering the surface of the target goes into a stoichiometrical equilibrium of all components included in the target. This equilibrium is important to produce high quality films, otherwise the composition of the grown film would not be the desired one.

4.2 X-Ray diffraction

X-ray characterization was performed with a high-resolution Bruker D8 Discover diffractometer, outfitted with a Göbel mirror and a two-bounce Ge(222) monochromator for the incident beam and a triple bounce or variable slit analyzer for the diffracted beam. Measurements were made with copper Kα_1 radiation ($\lambda = 1.5402$Å). In the diffractometer the x-ray source is fixed, leaving a sample rotation angle ω between the surface of the sample and the incoming beam, a detector rotation angle 2θ between the incoming beam and the detector, the angle Φ to rotate the sample around its surface normal and the angle χ which rotates the sample around the axis which is perpendicular to the surface normal. Fig. 9 shows the schematic alignment of the x-ray diffractometer with the four angles $(\omega, 2\theta, \chi, \Phi)$. The difference between ω and θ is that ω is the angle between the incoming x-ray beam and the surface of the sample and θ is the

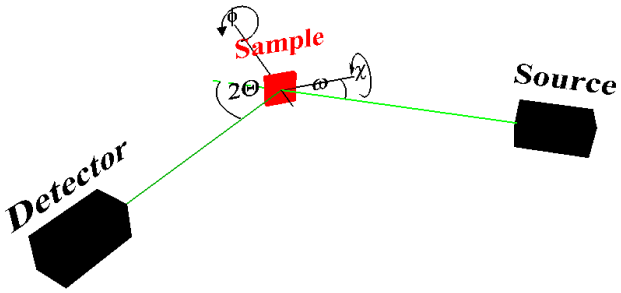

Figure 9: Schematic geometry of the X-ray diffractometer with the four angles $(\omega, 2\theta, \chi, \Phi)$. ω is the angle between the surface and the incoming x-ray beam, 2θ is the angle between the detector and the incoming x-ray beam, Φ rotates the sample around the surface normal and χ rotates the sample around the axis which is perpendicular to the surface normal.

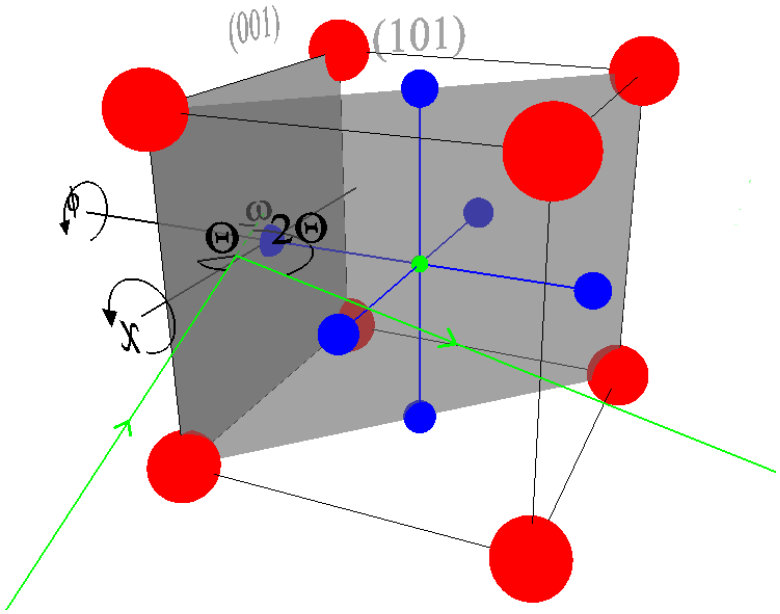

Figure 10: X-ray diffraction on the (101) plane with the (001) plane as surface plane and the four angles $(\omega, 2\theta, \chi, \Phi)$ of the x-ray diffractometer. The planes in the image are real space representations of the diffraction planes, which are defined in reciprocal space.

angle between the incoming x-ray beam and the diffraction, or Bragg plane. To illustrate this difference Fig. 10 shows the diffraction planes from inside the sample with the (001) plane as surface and the (101) plane as diffraction plane. One has to be careful since diffraction planes are defined in reciprocal space so the planes in Fig. 10 are real space representations of the corresponding diffraction planes. Most measurements were made in the (001) plane in which $\omega = \theta$. The angles χ and Φ can be used to correct misalignments of the sample.

The following subsection will give a short overview on some x-ray scan techniques. These methods, among many others, are explained with more detail in [31].

4.2.1 Rocking curve

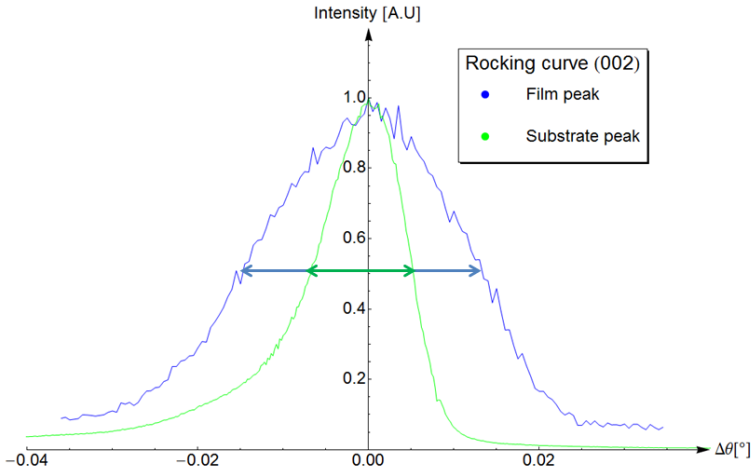

Figure 11: The image shows the rocking curves of a substrate and the film which was grown on it. The FWHM of the substrate is 0.012° and for the film it is 0.027°. This shows that the film did not grow with quite the same crystalline perfection as the substrate underneath it, though it is still a very high quality film.

During a rocking curve scan one changes the ω angle but keeps the 2θ angle constant. There are two motivations for rocking curve scans. One is the measurement of the ω offset, which is a consequence of the sample misalignment. The other motivation is to determine the defectiveness of substrates and films. Structural defects will widen the peak or even create additional peaks. Therefore one should compare the full width at half maximum (FWHM) of the substrate with the FWHM of the film rocking curve. It is a sign of perfect single crystal grown films if the FWHM of both, film and substrate, rocking curves are the same. Fig. 11 shows the rocking

curve of a $PbTiO_3$ film on a $SrTiO_3$ substrate. The FWHM of the rocking curve is 0.012° and for the film the FWHM is 0.027°. This means that the film does not have quite the same crystalline perfection as the substrate it was grown on, though it is still a very high quality film.

4.2.2 $2\theta - \omega$ scans

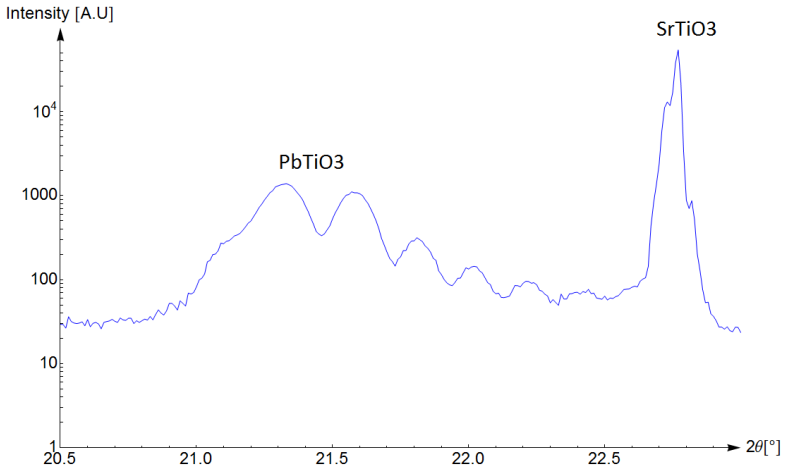

Figure 12: A $2\theta - \omega$ scan for a $PbTiO_3$ film. The sharp and high intensity peak is the $SrTiO_3$ substrate peak. The lower intensity peaks at lower 2θ angles are the *Laue oscillations* of the $PbTiO_3$ film. From this diffraction pattern one can estimate the film thickness, $t = 461$Å, and its value for $c = 4.157$Å.

With a $2\theta - \omega$ scan one can measure the lattice parameter, c, of a c-axis oriented film. To do so one searches for the (001) peak of the film and uses Bragg's law:

$$2d\sin(\theta_n) = n\lambda \tag{10}$$

with d=c (for the (001) peak) as the distance between two Bragg planes, n is the diffraction order, θ_n is the measured $\frac{2\theta}{2}$ angle for the nth diffraction order and λ is the wavelength of the x-ray source (In this thesis the Cu Kα_1, $\lambda = 1.5402$Å, line was used). If one wants to determine the lattice parameter c from the (00l) peak one has to use the inter plane distance $d = \frac{c}{l}$.

To determine the number of unit cells one can use the intensity oscillations around the peak. This oscillations are called *Laue oscillations* and can be calculated with the structure factor of

the crystal:

$$S_c(\vec{k}) = S_{uc} \cdot \frac{\sin(\vec{k} \cdot \vec{a}_j N)}{\sin(\vec{k} \cdot \vec{a}_j)} \tag{11}$$

here S_{uc} is the structure factor of the unit cell, $\vec{a}_j$ are the basis vectors of the atoms in the unit cell and N is the number of unit cells. By fitting the theoretical diffraction pattern to the measured (see Fig. 12) one can estimate the thickness $t = c \cdot N$ of the film. The thickness of the film in fig. 12 is $t = 461$Å the estimated value for $c = 4.157$Å.

4.2.3 Low-angle reflectometry

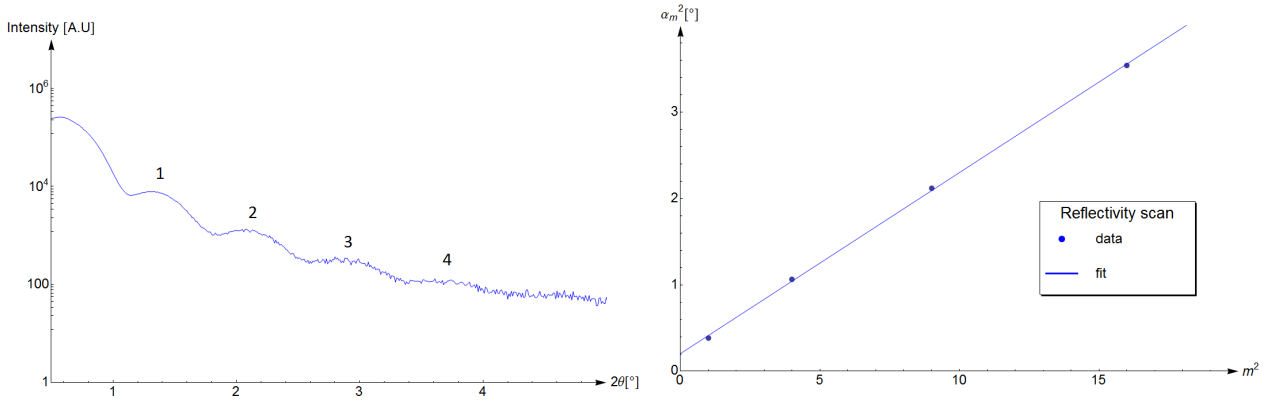

Figure 13: On the left side the low angle reflectometry scan is shown. The numbers refer to the reflection order m. On the right side α_m^2 is plotted against m^2 together with the best linear fit to the data. The thickness for the shown $PbTiO_3$ film is t=8nm.

Another method to determine the thickness of a film is the low-angle reflectometry. It is also a $2\theta - \omega$ scan, but this time with a low ω angle. In this method one measures intensity oscillations, which are caused by interference of the reflected beam at the surface and the reflected beam at the interface between the film and the substrate. The intensity maxima can be calculated by:

$$2t\sqrt{\sin(\alpha_{im})^2 - \sin(\alpha_c)^2} = m\lambda \tag{12}$$

where t is the thickness of the film, α_{im} is the angle of the mth intensity maximum, $\sin(\alpha_c) = \sqrt{2(1-n)}$, α_c is the critical angle of total external reflection, n is the refractive index of the film and m is the order of the maximum.

The low-angle reflectometry is done at low incident angles α_{im}, therefore one can make a low

angle approximation for the $\sin(\alpha_{im})$ and $\sin(\alpha_c)$ in eq. (12).

$$\alpha_{im}^2 = \left(\frac{m\lambda}{2t}\right)^2 + \alpha_c^2 \tag{13}$$

One can use this approximation to determine the thickness of a film graphically, by plotting α_{im}^2 against m^2. With the slope, $s = (\frac{\lambda}{2t})^2$, of this plot one can calculate the thickness, $t = \frac{\lambda}{2\sqrt{s}}$, for a film. Furthermore one can get α_c^2 as the offset on the α_{im}^2 axes. With α_c one can calculate the refraction index $n = 1 - \frac{\sin(\alpha_c)^2}{2}$. In Fig. 13 this method was used to determine the thickness of a $PbTiO_3$ film to t=8nm.

4.3 Atomic force microscopy

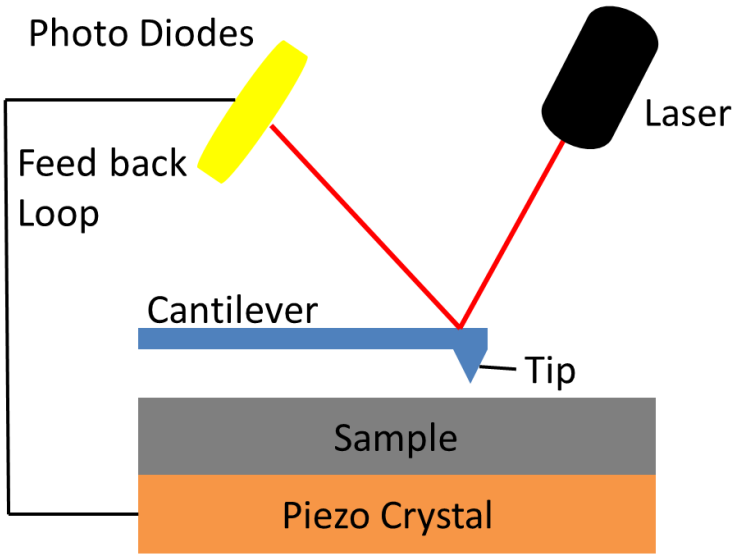

Figure 14: Schematic of an Atomic Force Microscope (AFM). The tip is placed on a cantilever and a photodiode array measures the deflection of the tip. Piezo crystals under the sample can move the sample in all space dimensions.

The Atomic Force Microscope (AFM) was invented by Binnig, Quate and Gerber in 1986[2]. It is used to make images of surfaces on the nm scale. For this thesis an Asylum Research MFP-3D-SA AFM was used.

The AFM uses atomic forces (van der Waals forces, capillary forces, chemical bonding,

electrostatic forces, etc.) to measure the surface of a sample. The atomic forces are measured with a small tip, ideally with a single atom at the end, which is held by a cantilever. The sample can be moved by piezo crystals, which are placed below the sample, in all space dimensions. Furthermore a laser is reflected by the top surface of the tip (see Fig 14) into an array of photodiodes. With the signal of the photodiodes one can measure the deflection of the tip. There are different modes in which on can use the AFM. One of these methods will be the topic of the next subsection.

4.3.1 Topographic measurements (non contact mode)

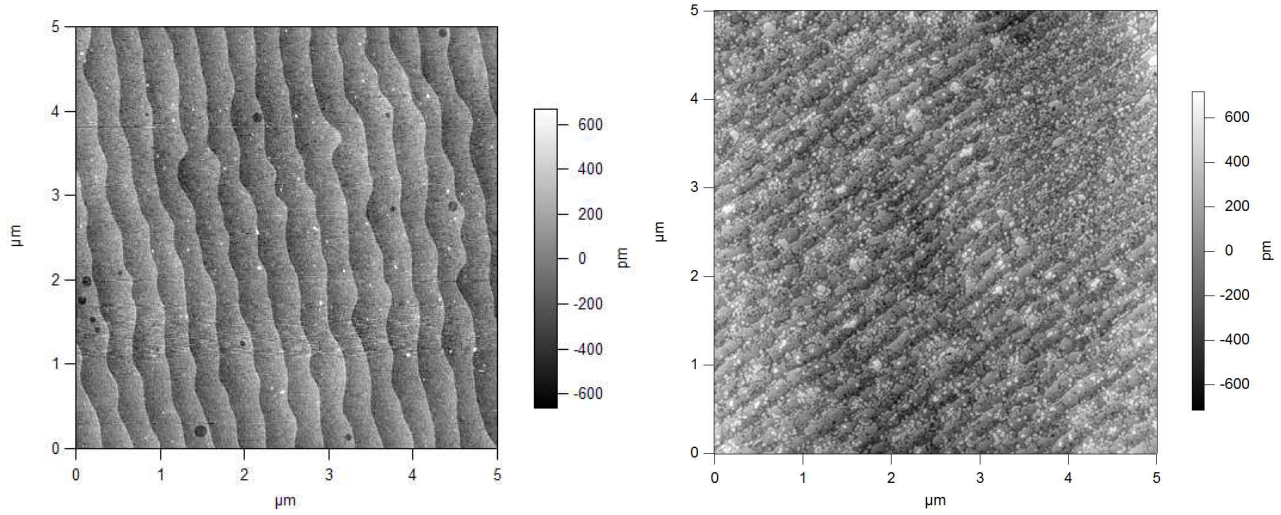

Figure 15: The image shows on the left side a $SrTiO_3$ surface. One can see the single unit cell steps very clearly. On the right hand side a 10nm thick $PbTiO_3$ film is shown. It also has a smooth surface but not as smooth as the substrate surface.

In a topographic scan the tip first gets tuned close to its resonance frequency (usually $\approx -10\%$ off). Now the tip is brought close to the sample, in the range of atomic forces. Afterwards the tip is rastered in the x and y directions over the sample. While the tip is moving the, height of the surface changes, and with the height also the atomic forces. One tries to keep the atomic forces between the tip and the surface constant by moving the sample up and down (z direction) with the piezo crystal underneath it. The final topographic image is a reconstruction of the z adjustments. With this technique one can measure the step edges of perovskite crystals (See Fig. 15. The height of the step edges is $\approx$4Å). Topographic scans were also used to measure

the number and the height of deposited silver spots on different surfaces.

4.4 Silver deposition

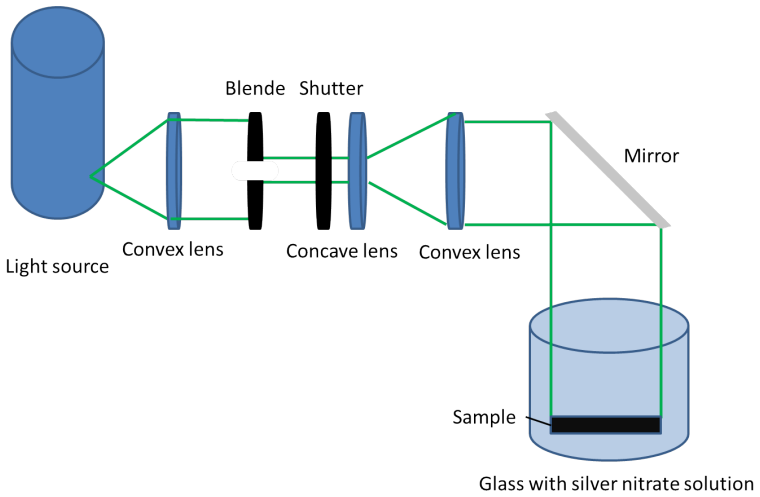

Figure 16: Schematic of a experimental setup to deposit silver on thin films. First the light of the UV lamp is collected into a parallel light beam. Then a part of the beam is transmitted into a blende. In the end the beam is widened to reduce the intensity per m^2. The shutter is used for a good control of the illumination time

To deposit silver on $SrTiO_3$ or $PbTiO_3$ one needs a simple experimental setup. The basic setup is a UV light source and a sample in $AgNO_3$ solution. To get a good control over the silver deposition one needs a good control over the incoming radiation. Most UV lamps are very intense, and if one wants to measure the deposition of silver in the early stage, the intensity must be reduced. For this reason one can use a more complex experimental setup like in Fig. 16, where a part of the radiation is dumped into a blende and afterwards the beam is widened. With a shutter one has a good control over the illumination time. To get an estimate of which materials are more reactive, one can compare the amount of deposited silver on two different materials after the same illumination time in an identical silver nitrate solution.

To investigate the spectral characteristic of the silver deposition one can use a prism and illuminate one sample with different wavelengths simultaneously. This could result into a silver gradient for different wave lengths and one might be able to get an estimation of the band gap.

5 Reaction Diffusion Model

To model the growth of silver spots on ferroelectric surfaces a reaction diffusion model was used. In this model one can estimate the number of silver atoms accumulated on one spot from the spot height. To do so one has to calculate the silver density inside the spot ρ(r) depending on the radius of the spot. This density decays with a power law of $r^{-0.58}$ and has finite size effects. First the basic principles of the model will be described. Afterwards a way to estimate the density, ρ(r), will be introduced.

5.1 Basic Principles

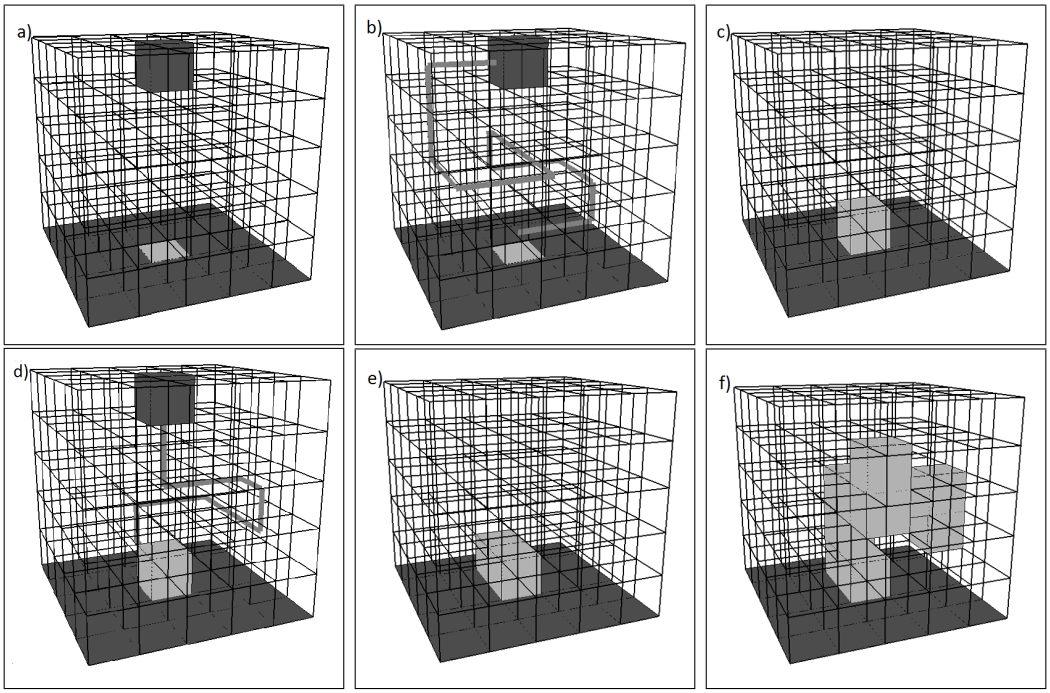

Figure 17: The images show the model growth of a silver spot. Fig. a) shows the grid with one active site on the bottom of the grid (active site are light gray) and one starting silver atom on top. during the simulation the atoms can not move through the dark gray area on the bottom, but in the other two dimensions the model has periodic boundaries. The atoms get initialized at the top of the grid and randomly in the x and y direction. Fig. b) shows in light gray one possible path of the atom through the grid. Fig. c) shows the new active area after the first atom got adsorbed on the surface. Fig. d) show the initialization and possible movement of a second atom. Fig. e) shows the active area after two atoms got adsorbed. Finally fig. f) shows the active area after several atoms got adsorbed.

The model used is a simple reaction diffusion model. The simulation starts with an empty 3 dimensional grid. The grid has periodic boundary conditions in two dimensions and in the third dimension it has a fixed boundary condition. Fig. 17 a) shows an empty grid with one active cell on the bottom in light gray and one atom on the top of the grid. The dark gray area on the bottom illustrates the fixed boundary. At the beginning of a simulation one atom gets created at the top of the grid, its x and y positions are initialized randomly. Now the atom moves randomly through the grid until it is next to an active area. Active areas are highlighted in all pictures with a light gray color. In Fig. 17 b) the light gray line illustrates the random path an atom could take through the grid. When the atom is next to an active site the atom becomes fixed and now the surface of the atom is active, increasing the active area. Figure 17 c) shows the active area after one atom is adsorbed. After a atom is adsorbed the next atom is created on the top of the grid and with random x and y coordinates. Now the atom is moved randomly similarly to the first (shown in in fig. 17 d)). Fig. 17 e) shows the new active area after two atoms are fixed. New atoms are created and moved until one wants to stop the simulation. Fig. 17 f) finally shows a small spot of adsorbed atoms. In these simulations the size of one cell in the grid can be interpreted with the binding length between the occupant atoms. This means the simulation can not predict an exact value of silver atoms for one spot from its height, if one does not know the binding length between the atoms. But with this model one can compare two different spots and estimate the relative amount of silver of the two spots and finally a comparison between two different samples.

5.2 Density

To calculate the density of a spot, one begins the simulation with a single active cell. From the diffusive nature of the model one expects that the spot grows in a half sphere around the active cell. This means that the density has a spherical symmetry around the active cell. Since a square lattice is used in the simulation one has to choose which cells belongs to which sphere shell. In this simulations the sphere shells are defined by $r^2 \geq x^2 + y^2 + z^2$ and $(r-1)^2 \leq x^2 + y^2 + z^2$, where x, y and z refer to the site coordinates, with respect to the seed, in the square lattice. One effect of the discretization is that one can simulate ρ(r) only for r as integer multiple of the lattice cell length. This leads to an large error for small radii. Furthermore, the density for

small radii could be dependent on the type of lattice one uses. Therefore, one is more interested in the development of the density for large r. Unfortunately there are finite size effects of the density when r reaches the spot height R. This means if the spot grows to a specific height R, one observes an exponential decay of the density close to the specified height R. Fig. 18 shows the density, ρ(r), for different spot heights, R, and the fitted functions to the data. One can see that the density first falls with a power law until the finite size effects begin to dominate. This means the density ρ is dependent on the height of a spot R. Now one would like to have a function ρ(r, R) which fits the density for all spot heights, this can be calculated by the piecewise defined function (14). If one knows the crystal structure of the deposited silver, one might find that another lattice would model the spots better.

$$\rho(r,R) = \begin{cases} \frac{r^{0.58}}{2.3} & if \quad r < 0.45R \\ \frac{r^{0.58}}{2.3} \cdot \exp(-\frac{(r-0.45R)^2}{\sqrt{R^3}}) & else \end{cases} \tag{14}$$

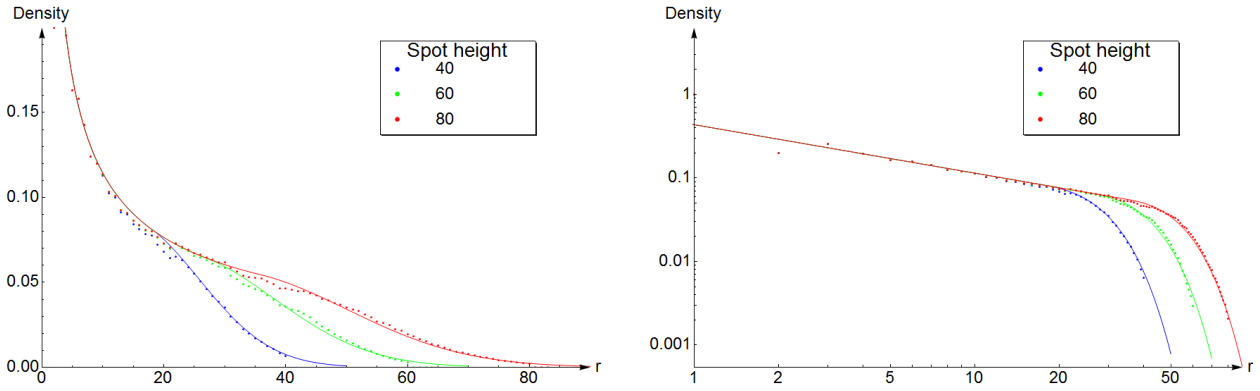

Figure 18: The figure shows a linear plot (on the left) and a loglog plot (on the right) of the simulation data (points) and the fitted partial defined function (lines). The colors refer to the height of the spot.

Another function that can fit the data is a stretched exponential function (15). Te corresponding graphs are shown in fig. 19. The first fit (14) is a better fit to the data but a piecewise defined function might not be the best way to fit the data. The stretched exponential fit (15) can also fit the simulation data and is one closed function, but the fit is not as good as the one

for the piecewise defined fit (14)

$$\rho(r,R) = \frac{r^{0.58}}{2.3} \exp\left(-\left(\frac{r}{7+R*0.7}\right)^{4.8}\right) \tag{15}$$

Fig 19 shows the stretched exponential fit together with the simulation data. The simulation data was collected in 300x300x300 grid and the density is averaged over 20 spots. With more computational power one could simulate the density for higher spots. One could also look for finite size effects resulting from the grid size by simulating the spot densities for different grid sizes and constant spot heights.

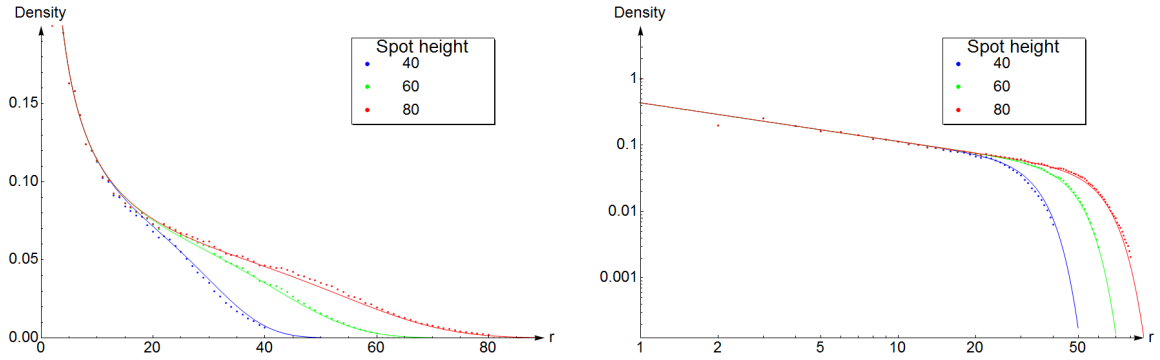

Figure 19: The figure shows a linear plot (on the left) and a loglog plot (on the right) of the simulation data (points) and the fitted stretched exponential function (lines). The colors refer to the height of the spot.

6 Spot counting

To measure the reactivity of different materials one needs to be able to estimate the amount of silver deposit on different samples. To do so one can measure the number and the height of the silver spots on a material. To measure the height of the spots is easily done with an AFM (see section 4.3), but to count the number of spots on an AFM image is more difficult. For this reason one of the goals of this work was to write a program which can count the number of spots. This section will introduce the functions of this program and explain how to use it.

6.1 Basic operations

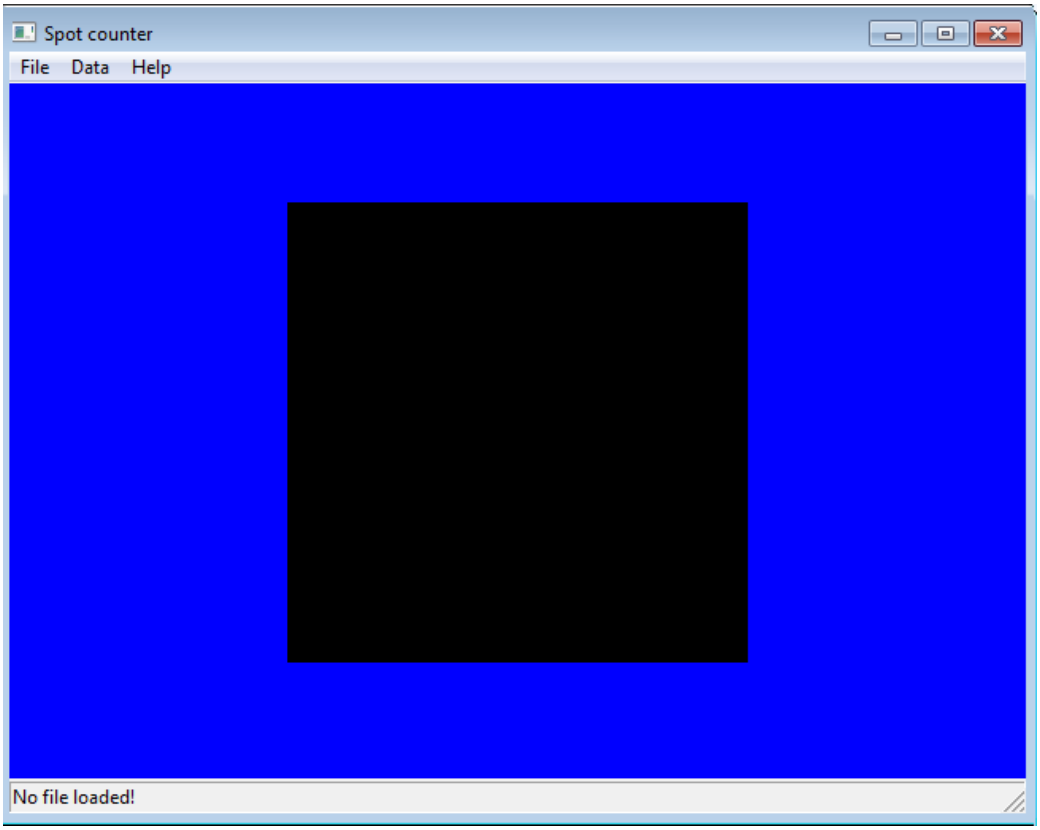

Figure 20: Picture of the window after starting the program. The status bar in the bottom displays the currently open file name. The black square in the center of the window is the area where an image of the data is displayed.

Fig. 20 shows the Spot counter program. At the top of the window is the menu, which will be described in more detail in section 6.2. In the bottom of the window is the status bar which

Key	Response
a	moves the displayed data to the left
d	moves the displayed data to the right
w	moves the displayed data down
s	moves the displayed data up
q	zooms into the data
e	zooms out of the data

Table 1: Summarization of the program response to keyboard input.

displays the path and file name of the active file. The main part of the window is filled with blue and a black square. The black square is the area where an image of the data will be displayed. To move the displayed data and zoom in and out one can use the keyboard (see table 1).

After the data is loaded and the spots are counted, one can select a single spot by clicking on it with the mouse and get its information from the Spot Info dialog (see section 6.3.3).

6.2 Menu

The Menu contains of three sub-menus. The Help sub-menu only contains an about box.

The Data sub-menu (see Fig. 21) contains the option to begin counting spots. The method

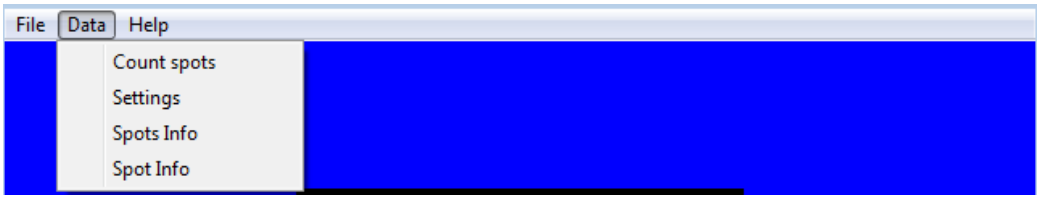

Figure 21: Menu to work on the data and open the display dialogs.

how the spots are counted is described in detail in section 6.4. One can also open the Settings dialog box which is described in section 6.3.1 to setup the correct values for the spot counting method. The Spot Info menu point opens the Spot Info dialog box (See section 6.3.3). The last menu point is Spots Info, which opens the Spots Info dialog box (see section 6.3.2). The Spot info dialog shows information about one single spot, while the Spots Info dialog box shows average information about all counted spots.

In the file menu one opens plain text files of the measured AFM data. It is important

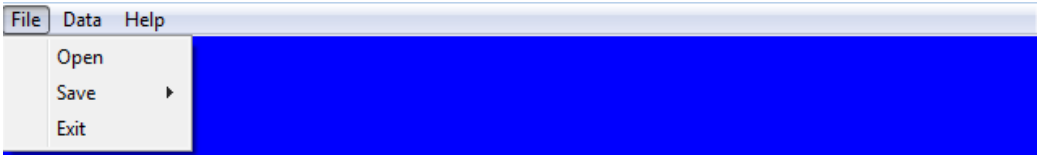

Figure 22: Menu to open files and save some information about the counted spots.

that one only opens AFM data which has 512X512 data points; otherwise the program will not work! After hitting the open button an open dialog appears and one can choose the file to open. Opened files must also have the extension '.afm'. The extension helps to distinguish the AFM data files more easily from other files. The program can save the heights and areas of the spots to a plain text file. In these files each line contains the height or area value of one spot. The Exit menu point will close the program.

6.3 Dialogs

This section is a short summary of the program dialog boxes. The dialogs are used to set up the variables for the spot counting method and to display information about a single spot or about all spots.

6.3.1 Settings

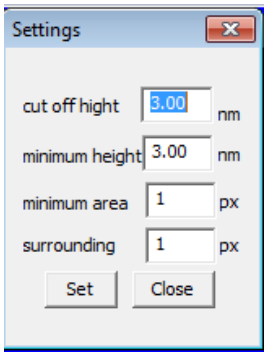

Figure 23: The Settings dialog box can be used to set the *cut off height*, the *minimum height* for active spots, the *minimum area* for active spots and the area in which the method searches for pixels to add them to a spot(*surrounding*).

The Settings dialog box is shown in Fig.23. One can enter four variables. The first is the *cut off height*. Only points higher than the *cut off height* are counted in the spot counting method (see section 6.4). The area of a spot is the number of pixels which are above the *cut off height* and are counted as one spot. The *minimum height* is the minimal height a spot has to have to be counted as active. If no point of a spot is higher than the *minimum height* it gets labeled as inactive and will not be displayed on the screen. Also, inactive spots get assigned a spot ID (a unique ID which is used to distinguish spots easier). The *minimum area* is the number of points a spot must have to be counted as active. Finally *surrounding* defines the area in which the spot counting method searches for points above the *cut off height* to add them to one spot. After changing the *cut off height* or *surrounding* one has to recount spots. In contrast the *minimum height* and *minimum area* can be changed without recounting the spots.

6.3.2 Spots Info

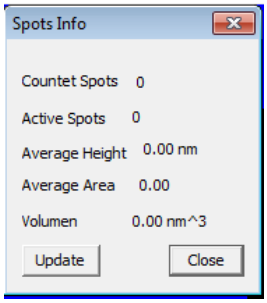

Figure 24: The Spots Info dialog box displays information about all counted spots on the image.

The Spots Info dialog displays information about all counted spots on the image and is shown in Fig. 24. The displayed information is the total number of counted spots, the number of active spots (see section 6.3.1 for a description which spots are counted as active.), and the average height and area of the active spots. The last displayed information is the volume of the active spots based on an the approximation that they grow in half-spheres with the density of the Diffusion Reaction model from section 5. The volume is the best way to compare two different samples that could be found in this thesis.

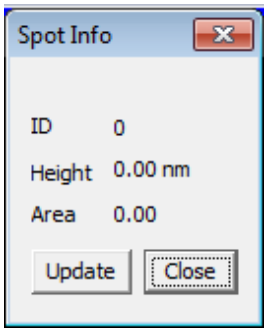

Figure 25: The Spot Info dialog box displays the spot ID, height and area off the selected spot.

6.3.3 Spot Info

The Spot Info dialog displays the spot ID, height and area of the selected spot and is shown in Fig.25. To select a spot one has to click with the mouse on the spot he wants to select. If two spots are very close, one should first zoom in, otherwise the wrong spot might be selected.

6.4 Counting Spots

The spot counting method takes the values of the *cut off height* and *surrounding* which has been defined in the Settings dialog (see section 6.3.1). Surrounding defines the radius, in pixels, of a circle around each point, in which the spot counting method is searching for points above the *cut off height* to add them to one spot. The circle is defined by:

$$x^2 + y^2 \leq r^2 \tag{16}$$

where x is the distance from the current point in the x direction, y is the distance from the current point in the y direction and r is the value of *surrounding*. Fig. 26 shows the necessary values of *surrounding* to add points to the one in the middle.

The spot counting method starts to search for spots in the upper left corner and goes through the data line by line. When it approaches a point above the *cut off height* it searches in the circle defined by the *surrounding* value for a point which already has a spot ID. If it can find a point with a spot ID it gives the current point the same ID, otherwise it assigns the current point a new spot ID. If there are two different spots (with different spot IDs) in the surrounding

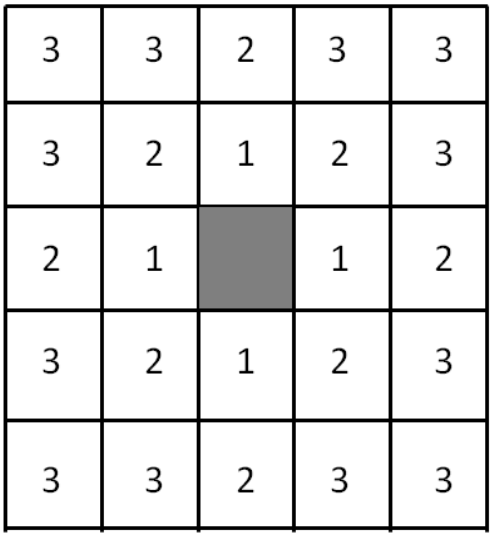

Figure 26: The image shows the area in which the spot counting method counts points around another point to the same spot. If the value of *surrounding* is greater or equal to the number in a lattice site, all these points would be counted to the same spot, if there height is above the *cut off height*.

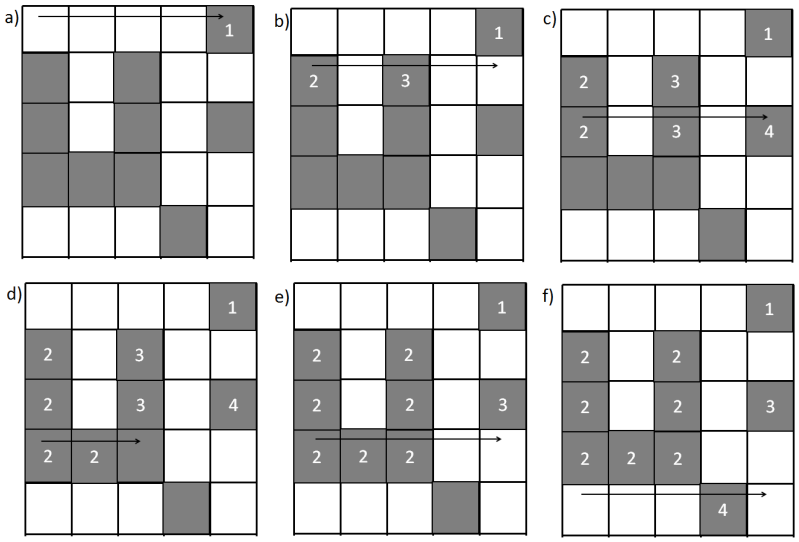

Figure 27: The figure shows how the spot counting method works. It goes through the data starting at the top left corner and goes line by line through the data. It assigns each new spot a new unique spot ID. When the method finds a connection between two different spots, it merges both spots two one with the same spot ID and corrects all other spot IDs.

circle the spot counting method merges these two spots to one spot with the lower spot ID. All spots which have a spot ID which is greater than the higher spot ID get their spot ID reduced by one. In the end the greatest spot ID is equal to the number of spots.

To better understand the spot counting method, it can be explained with a small example in which the value of *surrounding* is set to one. Take a data set which is 5x5 pixels large and, for illustration, all pixels above the *cut off height* are filled with a gray color. Fig. 27 a) shows the data and the assigned spot IDs after the method has finished the first line. Only the point in the upper right corner has a spot ID. Fig. 27 b) shows the data after the method has scanned the second line. Now there are two new spots with the IDs 2 and 3. While the method scans the third line it ads one point to the second spot, one to the third spot and it finds a new spot with the spot ID 4 (Shown in Fig. 27 c)). In Fig. 27 d) the method just reaches the third point and finds two different spots next to it. Now the method merges both spots with ID 2 and 3 to one spot with ID 2 and corrects the spot ID for the fourth spot to 3. This is shown in Fig. 27 e). Finally Fig. 27 f) shows the example after the spot counting is finished now there are 4 different spots counted.

6.5 Saving AFM data to plain text

To save the AFM data to a plain text file one first opens the data file one wants to save. Then, select the data set one wants to export (Height Retrace, Phase, Z-Sensor,...). While the window with the data is selected in Igor Pro one has to press "Ctrl+J", selecting the Igor pro prompt. The command to save the data is "ExportAsText()", which opens a save dialog and one can choose the file name and path where the data will be saved. The saved text file contains all data points in one line.

7 Silver deposition on Perovskite crystals

To compare the surface reactivity of different perovskite crystals the following conditions were used during the silver deposition. The samples were illuminated with a 250W Hg-Xe lamp. The current through the lamp was 1.5A and the $AgNO_3$ solution was 0.00188 molar. Each sample was illuminated for 15 seconds. After the silver deposition the surface of the samples was examined with topographical AFM scans and for the statistical data the average of four 2.5x2.5 μm^2 areas was taken. The following sections show some topographical images and statistical data for the silver deposition on $SrTiO_3$ and $PbTiO_3$.

7.1 $SrTiO_3$

In this thesis (001) oriented TiO_2 terminated $SrTiO_3$ substrates are used. In the past work was done to investigate the influence of surface orientation for $SrTiO_3$ [7], and the authors showed that the (001) surface is the most reactive one.

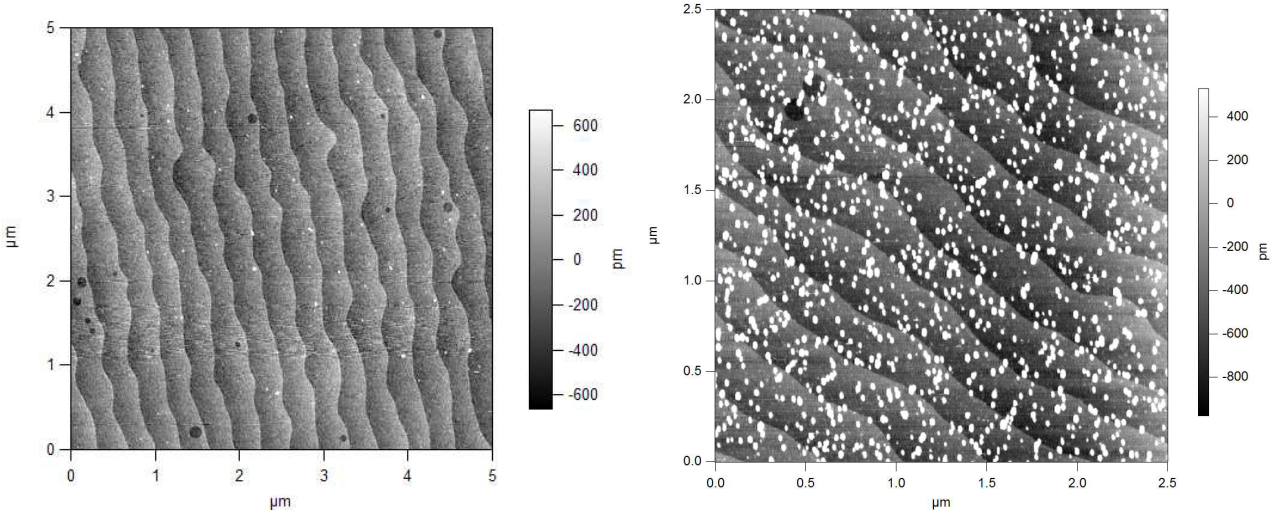

Figure 28: The image on the left side shows the $SrTiO_3$ surface before it got illuminated in the $AgNO_3$ solution. The image on the right side shows the surface of the sample after the silver deposition.

Fig. 28 shows AFM images of a sample before and after it got illuminated in a $AgNO_3$ solution. The average number of spots on this sample is 813±196 on a 2.5x2.5μm^2 area. The spots have an average height of (5.6±0.4) nm. The AFM also measures the area of the spots

but this area is a convolution between the AFM tip and the spot structure. The used tip has an diameter of ∼10nm and therefore the area of the spots is dominated by the shape of the tip. Nevertheless there is a linear correlation between the spot height and its measured area; this correlation is shown on the left side of Fig. 29. One can see that, especially for small heights, the graph has a linear dependence. For a greater spot height more points do not fit onto the line. This effect arises from the fact that two spots which are close to each other and have an overlapping area in the AFM image are counted as one spot. These spots have a greater area than they should have for their height and are located above the line. On the right side of Fig. 29 one can see the height distribution for this sample.

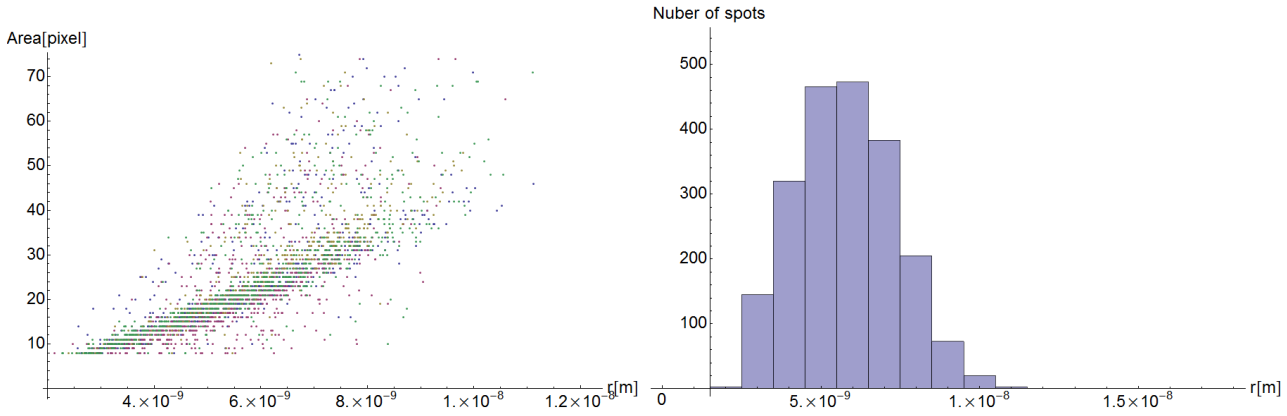

Figure 29: The image on the left side shows the area-height plot of silver spots on $SrTiO_3$ and on the right side one can see the histogram of the silver spot heights.

It was also observed that some $SrTiO_3$ samples have an enhanced silver growth on their step edges. Fig. 30 shows an AFM image of one of these samples. Since both substrates, the one with step edge enhanced growth (Fig. 30) and the one with random growth (Fig. 28), are from the same substrate box we could not determine the reason for the enhanced silver growth on step edges. This will be done in further experiments. Also, the growth on the step edges made it hard to distinguish between spots on the AFM image; it was not possible to do a reasonable comparison between the amount of silver deposited in the two different growth modes.

That silver grows in small spots instead of layers on $SrTiO_3$ was also predicted by DFT calculations [35].

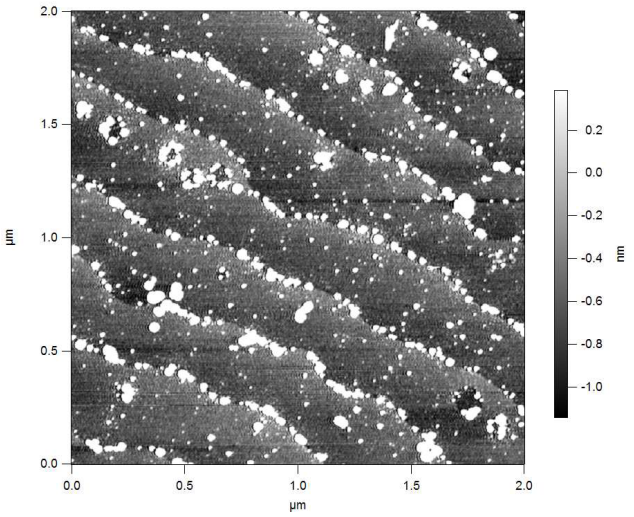

Figure 30: The image shows AFM measurements of $SrTiO_3$ after illumination. It can be seen that the step edges are enhancing the silver deposition on this sample.

7.2 $PbTiO_3$ on $SrTiO_3$

The same experiments as for $SrTiO_3$ were done on a ∼10nm thick $PbTiO_3$ film, which was grown with the sputtering technique described in section 4.1. In [27] the authors showed with x-ray diffraction that the deposited particles on the $PbTiO_3$ film are silver particles.

Fig. 31 shows AFM images of a $PbTiO_3$ film before and after it was illuminated in a $AgNO_3$ solution. The average number of spots on this sample is 411±10 on a 2.5x2.5μm^2 area. The spots have an average height of (8.2±0.2)nm. If one compares the amount of deposited silver between the $SrTiO_3$ and the $PbTiO_3$ one finds that on $PbTiO_3 \sim 50\%$ more silver was deposed than on $SrTiO_3$. The result is based on the diffusion reaction model from section 5 and has to be confirmed by other methods, if other methods come to the same result this would suggest that the used model describes the dominant part of the silver deposition process. The spots on the $PbTiO_3$ film could be measured more clearly, which can also been seen from the area vs. height plot on the left side of Fig. 32. On the right side of Fig. 32 the height histogram is shown. On $PbTiO_3$ there are less spots than on $SrTiO_3$, but the spots have a greater height than the ones on $SrTiO_3$.

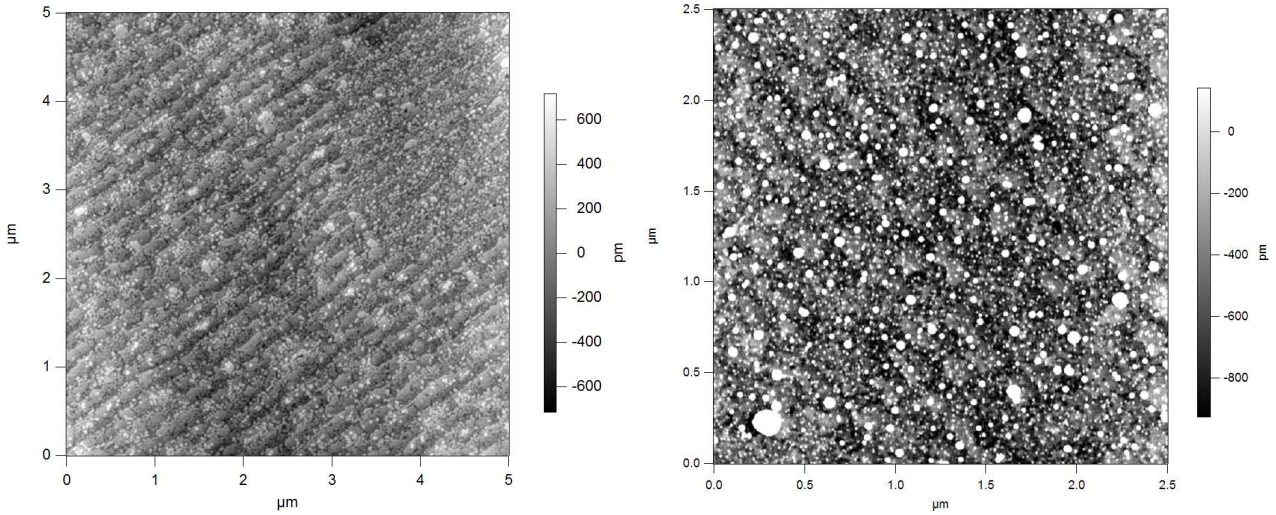

Figure 31: The image on the left side shows the $PbTiO_3$ surface before it got illuminated in the $AgNO_3$ solution. The image on the right side shows the surface of the sample after the silver deposition.

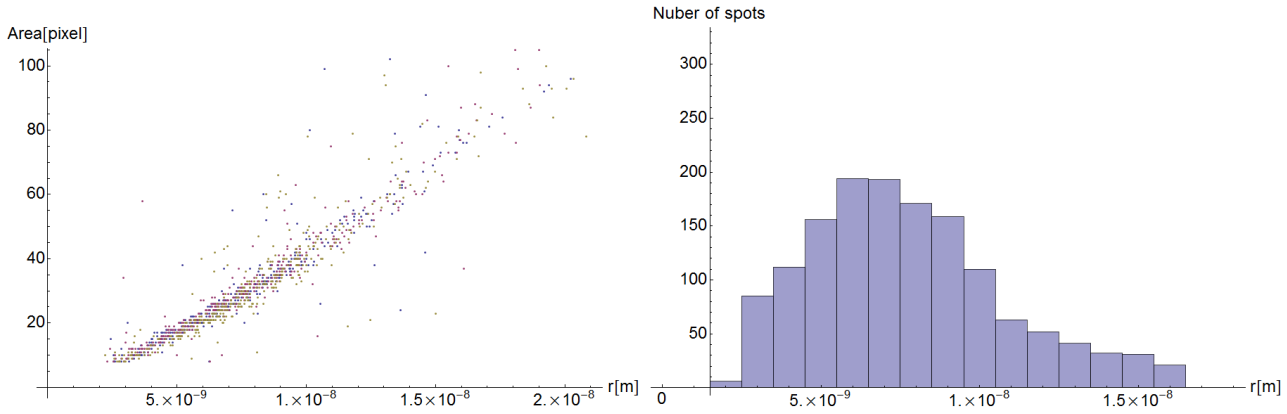

Figure 32: The image on the left side shows the area-height plot of silver spots on $PbTiO_3$ and on the right side one can see the histogram of the silver spot heights.

7.3 $PbTiO_3$ on $SrRuO_3$ on $SrTiO_3$

The experiment was repeated on a ∼10nm $PbTiO_3$ film on top of a ∼20nm $SrRuO_3$ bottom electrode to investigate if the electrode influences the silver deposition.

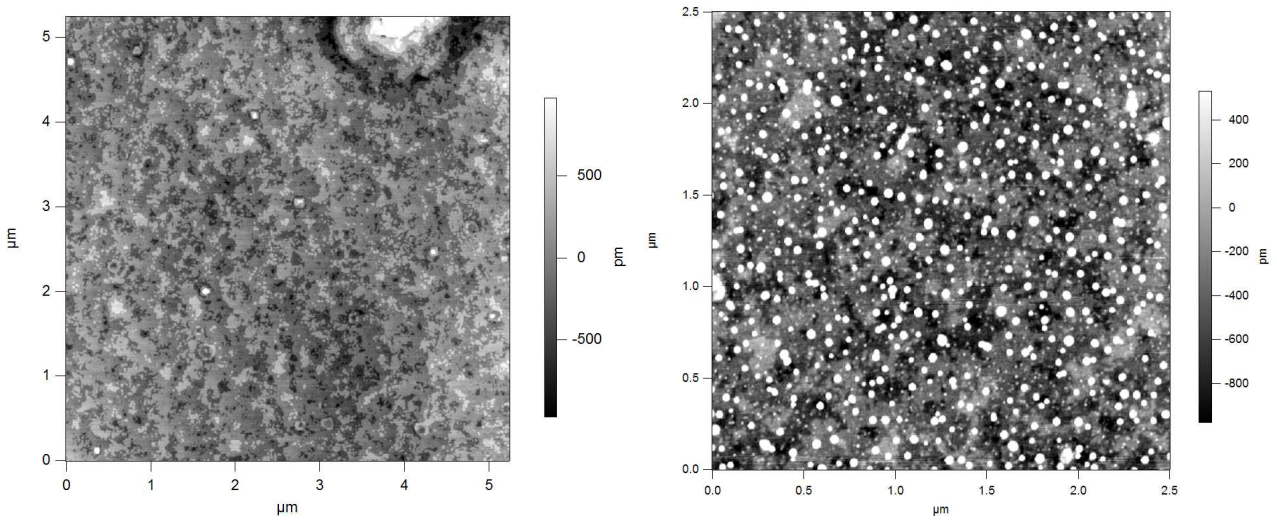

Figure 33: The image on the left side shows the $PbTiO_3$ on $SrRuO_3$ surface before it got illuminated in the $AgNO_3$ solution. The image on the right side shows the surface of the sample after the silver deposition.

Fig. 33 shows AFM images of a sample before and after it got illuminated in a $AgNO_3$ solution. From the images one can estimate the average number of spots on this sample is 412±113 on a 2.5X2.5μm^2 area. The spots have an average height of (8.3±1.2)nm. The amount of silver, based on the model of sec. 5, is the same as on $PbTiO_3$ without a bottom electrode. This leads to the conclusion that the bottom electrode has no influence on the surface reactivity of the $PbTiO_3$ film on top of it. The measured area-height correlations are shown on the left side of Fig. 34. The spot height area correlation is not as strong as on the plain $PbTiO_3$, which can also be seen in the higher statistical errors on this sample. Fig. 34 shows on the right side the height histogram of the sample, which is comparable to the one for $PbTiO_3$ without a bottom electrode (see left part of Fig. 32).

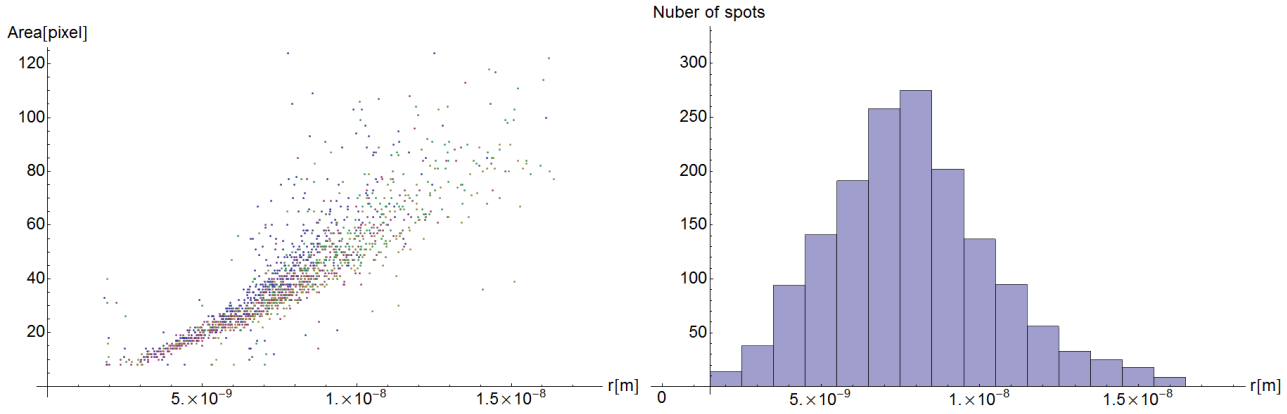

Figure 34: The image on the left side shows the area-height plot of silver spots on $PbTiO_3$ on $SrRuO_3$ and on the right side one can see the histogram of the silver spot heights.

8 Conclusion and perspective

In this thesis silver was photo catalytically deposed onto perovskite crystals. The silver was deposited as nano particles and measured with AFM Topography. Table 2 shows a summary of the statistical results for different materials.

Material	Spot height	Number of particles
$SrTiO_3$	(5.6±0.4)nm	813±196
$PbTiO_3$	(8.2±0.2)nm	411±10
$PbTiO_3$ on $SrRuO_3$	(8.3±1.2)nm	412±113

Table 2: Summary of the silver deposition experiment.

To process the AFM images and extract the appropriated data a program was written and its functionality is described in section 6. By applying a simple reaction diffusion model to the silver spot growth, an enhanced surface reactivity of 50% on $PbTiO_3$ compared to $SrTiO_3$ for the silver deposition reaction can be predicted. This result has to be confirmed by other techniques. Furthermore, it has been shown that the surface reactivity of $PbTiO_3$ is not influenced by an $SrRuO_3$ bottom electrode.

In future work a time resolved silver growth experiment is planned; these experiment can give an answer to the question of whether the silver growth gets enhanced after the first silver seeds are deposed on the surface. This can be done by measuring the amount of silver after a fixed period of time and illuminating the sample in a $AgNO_3$ solution again for the same time. After the second illumination one would measure the amount of deposed silver again and compares it to the first result. One could add more time steps to the experiment to increase the accuracy of the results.

The final goal of these experiment is to find new materials to split water under visible light. A lot of work has been done on visible light reactivity of doped $SrTiO_3$ and is summarized in sec. 3.5. Another planned experiment is to illuminate ferroelectric super lattices with visible light absorption and to probe if they are able to split water on their surface.

To investigate the influence of ferroelectricity on the surface reactivity one can write domains onto the sample and measure how this influences the silver deposition on top of the domains.

References

[1] MD ARCHER and JR BOLTON. REQUIREMENTS FOR IDEAL PERFORMANCE OF PHOTOCHEMICAL AND PHOTOVOLTAIC SOLAR-ENERGY CONVERTERS. *JOURNAL OF PHYSICAL CHEMISTRY*, 94(21):8028–8036, OCT 18 1990.

[2] G. Binnig, C.F. Quate, and C. Gerber. Atomic force microscope. *Physical review letters*, 56(9):930–933, 1986.

[3] JR Bolton. Solar photoproduction of hydrogen: A review. *SOLAR ENERGY*, 57(1):37–50, JUL 1996.

[4] A FUJISHIMA and K HONDA. ELECTROCHEMICAL PHOTOLYSIS OF WATER AT A SEMICONDUCTOR ELECTRODE. *NATURE*, 238(5358):37+, 1972.

[5] Gregory Geneste and Brahim Dkhil. Adsorption and dissociation of H2O on in-plane-polarized BaTiO3(001) surfaces and their relation to ferroelectricity. *PHYSICAL REVIEW B*, 79(23), JUN 2009.

[6] JL Giocondi and GS Rohrer. Spatial separation of photochemical oxidation and reduction reactions on the surface of ferroelectric BaTiO3. *JOURNAL OF PHYSICAL CHEMISTRY B*, 105(35):8275–8277, SEP 6 2001.

[7] JL Giocondi and GS Rohrer. Structure sensitivity of photochemical oxidation and reduction reactions on SrTiO3 surfaces. *JOURNAL OF THE AMERICAN CERAMIC SOCIETY*, 86(7):1182–1189, JUL 2003.

[8] VM Goldschmidt. The laws of crystal chemistry. *NATURWISSENSCHAFTEN*, 14:477–485, 1926.

[9] JH Haeni, P Irvin, W Chang, R Uecker, P Reiche, YL Li, S Choudhury, W Tian, ME Hawley, B Craigo, AK Tagantsev, XQ Pan, SK Streiffer, LQ Chen, SW Kirchoefer, J Levy, and DG Schlom. Room-temperature ferroelectricity in strained SrTiO3. *NATURE*, 430(7001):758–761, AUG 12 2004.

[10] SV Kalinin and DA Bonnell. Local potential and polarization screening on ferroelectric surfaces. *PHYSICAL REVIEW B*, 63(12), MAR 15 2001.

[11] H Kato and A Kudo. Visible-light-response and photocatalytic activities of TiO2 and SrTiO3 photocatalysts codoped with antimony and chromium. *JOURNAL OF PHYSICAL CHEMISTRY B*, 106(19):5029–5034, MAY 16 2002.

[12] R Konta, T Ishii, H Kato, and A Kudo. Photocatalytic activities of noble metal ion doped SrTiO3 under visible light irradiation. *JOURNAL OF PHYSICAL CHEMISTRY B*, 108(26):8992–8995, JUL 1 2004.

[13] I Kornev, HX Fu, and L Bellaiche. Ultrathin films of ferroelectric solid solutions under a residual depolarizing field. *PHYSICAL REVIEW LETTERS*, 93(19), NOV 5 2004.

[14] Akihiko Kudo and Yugo Miseki. Heterogeneous photocatalyst materials for water splitting. *CHEMICAL SOCIETY REVIEWS*, 38(1):253–278, 2009.

[15] Kazuhiko Maeda and Kazunari Domen. New non-oxide photocatalysts designed for overall water splitting under visible light. *JOURNAL OF PHYSICAL CHEMISTRY C*, 111(22):7851–7861, JUN 7 2007.

[16] B Meyer, J Padilla, and D Vanderbilt. Theory of PbTiO3, BaTiO3, and SrTiO3 surfaces. *FARADAY DISCUSSIONS*, 114:395–405, 1999.

[17] MP Moret, MAC Devillers, K Worhoff, and PK Larsen. Optical properties of PbTiO3, PbZrxTi1-xO3, and PbZrO3 films deposited by metalorganic chemical vapor on SrTiO3. *JOURNAL OF APPLIED PHYSICS*, 92(1):468–474, JUL 1 2002.

[18] A Munkholm, SK Streiffer, MVR Murty, JA Eastman, C Thompson, O Auciello, L Thompson, JF Moore, and GB Stephenson. Antiferrodistortive reconstruction of the PbTiO3(001) surface. *PHYSICAL REVIEW LETTERS*, 88(1), JAN 7 2002.

[19] R Niishiro, H Kato, and A Kudo. Nickel and either tantalum or niobium-codoped TiO2 and SrTiO3 photocatalysts with visible-light response for H-2 or O-2 evolution from aqueous solutions. *PHYSICAL CHEMISTRY CHEMICAL PHYSICS*, 7(10):2241–2245, 2005.

[20] T Ohsawa, K Nakajima, Y Matsumoto, and H Koinuma. Combinatorial discovery of anomalous substrate effect on the photochemical properties of transition metal-doped epitaxial SrTiO3 heterostructures. *APPLIED SURFACE SCIENCE*, 252(7):2603–2607, JAN 31 2006.

[21] K.M. Rabe, C.H. Ahn, and J.M. Triscone. *Physics of ferroelectrics: a modern perspective*. Springer Verlag, 2007.

[22] Krishnan Rajeshwar. Hydrogen generation at irradiated oxide semiconductor-solution interfaces. *JOURNAL OF APPLIED ELECTROCHEMISTRY*, 37(7):765–787, JUL 2007.

[23] G Rijnders, DHA Blank, J Choi, and CB Eom. Enhanced surface diffusion through termination conversion during epitaxial SrRuO3 growth. *APPLIED PHYSICS LETTERS*, 84(4):505–507, JAN 26 2004.

[24] Junsoo Shin, Von Braun Nascimento, Gregory Geneste, John Rundgren, E. Ward Plummer, Brahim Dkhil, Sergei V. Kalinin, and Arthur P. Baddorf. Atomistic Screening Mechanism of Ferroelectric Surfaces: An In Situ Study of the Polar Phase in Ultrathin BaTiO3 Films Exposed to H2O. *NANO LETTERS*, 9(11):3720–3725, NOV 2009.

[25] Junsoo Shin, Von Braun Nascimento, Gregory Geneste, John Rundgren, E. Ward Plummer, Brahim Dkhil, Sergei V. Kalinin, and Arthur P. Baddorf. Atomistic Screening Mechanism of Ferroelectric Surfaces: An In Situ Study of the Polar Phase in Ultrathin BaTiO3 Films Exposed to H2O. *NANO LETTERS*, 9(11):3720–3725, NOV 2009.

[26] V Subramanian, RK Roeder, and EE Wolf. Synthesis and UV-visible-light photoactivity of noble-metal-SrTiO3 composites. *INDUSTRIAL & ENGINEERING CHEMISTRY RESEARCH*, 45(7):2187–2193, MAR 29 2006.

[27] R. Takahashi, M. Katayama, O. Dahl, J. K. Grepstad, Y. Matsumoto, and T. Tybell. Epilayer control of photodeposited materials during UV photocatalysis. *APPLIED PHYSICS LETTERS*, 94(23), JUN 8 2009.

[28] R. Tanaka, S. Takata, M. Katayama, R. Takahashi, J. K. Grepstad, T. Tybell, and Y. Matsumoto. Photocatalytic Synthesis of Silver-Oxide Clathrate Ag7O8NO3. *JOURNAL OF THE ELECTROCHEMICAL SOCIETY*, 157(12):E181–E183, 2010.

[29] Divya Tiwari and Steve Dunn. Photochemistry on a polarisable semi-conductor: what do we understand today? *JOURNAL OF MATERIALS SCIENCE*, 44(19, Sp. Iss. SI):5063–5079, OCT 2009.

[30] T Tybell, CH Ahn, L Antognazza, and JM Triscone. Local analysis and modification of ferroelectric domain structures in thin films of Pb(ZrxTi1-x)O-3. *VIDE-SCIENCE TECHNIQUE ET APPLICATIONS*, 53(289):551+, 1998.

[31] T. Baumbach V. Holy, U. Pietsch. *High-Resolution X-Ray Scattering from Thin Films and Multilayers*. Springer Verlag, 1999.

[32] K van Benthem, C Elsasser, and RH French. Bulk electronic structure of SrTiO3: Experiment and theory. *JOURNAL OF APPLIED PHYSICS*, 90(12):6156–6164, DEC 15 2001.

[33] Defa Wang, Tetsuya Kako, and Jinhua Ye. New Series of Solid-Solution Semiconductors (AgNbO3)(1-x)(SrTiO3)(x) with Modulated Band Structure and Enhanced Visible-Light Photocatalytic Activity. *JOURNAL OF PHYSICAL CHEMISTRY C*, 113(9):3785–3792, MAR 5 2009.

[34] Defa Wang, Jinhua Ye, Tetsuya Kako, and Takashi Kimura. Photophysical and photocatalytic properties of SrTiO3 doped with Cr cations on different sites. *JOURNAL OF PHYSICAL CHEMISTRY B*, 110(32):15824–15830, AUG 17 2006.

[35] Wei Wei, Ying Dai, Meng Guo, Yingtao Zhu, and Baibiao Huang. Density Functional Theory Study of Ag Adsorption on SrTiO3 (001) Surface. *JOURNAL OF PHYSICAL CHEMISTRY C*, 114(24):10917–10921, JUN 24 2010.

[36] Wei Wei, Ying Dai, Hao Jin, and Baibiao Huang. Density functional characterization of the electronic structure and optical properties of Cr-doped SrTiO3. *JOURNAL OF PHYSICS D-APPLIED PHYSICS*, 42(5), MAR 7 2009.

[37] BM Wul and IM Goldman. Dielectric constants of titanates of metals of the second group. In *Dokl. Akad. Nauk SSSR*, volume 46, pages 154–57, 1945.